HHS Public Access

Author manuscript

Sci Immunol. Author manuscript; available in PMC 2019 December 21.

Published in final edited form as:

Sci Immunol. 2019 June 21; 4(36): . doi:10.1126/sciimmunol.aaw2004.

Intratumoral activation of the necroptotic pathway components RIPK1 and RIPK3 potentiates anti-tumor immunity

Annelise G. Snyder[1], **Nicholas W. Hubbard**[1], **Michelle N. Messmer**[1], **Sigal B. Kofman**[1], **Cassidy E. Hagan**[1], **Susana L. Orozco**[1,2], **Kristy Chiang**[2], **Brian P. Daniels**[3], **David Baker**[4], **Andrew Oberst**[1,*]

[1]Department of Immunology, University of Washington, Seattle WA 98109, USA.

[2]Molecular and Cellular Biology Program, University of Washington, Seattle WA 98109, USA.

[3]Department of Cell Biology and Neuroscience, Rutgers University, Piscataway NJ 08864, USA.

[4]Institute for Protein Design, University of Washington, Seattle WA 98109, USA.

Abstract

Although the signaling events that induce different forms of programmed cell death (PCD) are well-defined, the downstream immune responses to dying cells in the context of cancer remain relatively unexplored. Necroptosis occurs downstream of the receptor-interacting protein kinases RIPK1 and RIPK3, whose activation leads to lytic cell death accompanied by *de novo* production of pro-inflammatory mediators. Here, we show that ectopic introduction of necroptotic cells to the tumor microenvironment promotes $BATF3^+$ cDC1- and $CD8^+$ leukocyte-dependent anti-tumor immunity accompanied by increased tumor antigen loading by tumor-associated antigen presenting cells. Furthermore, we report the development of constitutively-active forms of the necroptosis-inducing enzyme RIPK3, and show that delivery of a gene encoding this enzyme to tumor cells using adeno-associated viruses (AAVs) induces tumor cell necroptosis, which synergizes with immune checkpoint blockade to promote durable tumor clearance. These findings support a role for RIPK1/RIPK3 activation as a beneficial proximal target in the initiation of tumor immunity. Considering that successful tumor immunotherapy regimens will require the rational application of multiple treatment modalities, we propose that maximizing the immunogenicity of dying cells within the tumor microenvironment through specific activation of the necroptotic pathway represents a beneficial treatment approach that may warrant further clinical development.

One Sentence Summary:

Activation of the necroptotic signaling kinases RIPK1 and RIPK3 within the tumor microenvironment enhances cDC1- and CD8+ leukocyte-mediated anti-tumor immunity.

*Corresponding author: oberst@uw.edu.

Author contributions: AGS and AO conceived the study and designed experiments. NWH designed AAV plasmid constructs. DB provided oligomerization domain constructs used in AAV experiments. AGS, NWH, MNM, BPD, SBK, CEH, SLO, and KC performed experiments. AGS and BPD analyzed data. AGS and AO wrote the manuscript with editorial input from all authors.

Competing interests: The testing of necroptosis-inducing AAVs was supported in part by funds received from FivePrime Therapeutics as part of a sponsored research agreement; AO has acted as a paid consultant for FivePrime Therapeutics. AGS, NWH, and AO are inventors on a pending patent held by the University of Washington for the constitutively-oligomerizing cell death enzymes described in this manuscript.

Introduction

Tumor immunotherapy, which boosts the ability of the body's own immune system to recognize and kill transformed cells, constitutes an immensely promising advance in the modern treatment of cancer. Notably, the efficacy of existing T cell-targeted therapies such as immune checkpoint blockade (ICB) can often be boosted upon co-administration of cytotoxic treatments such as irradiation (1,2). However, the specific forms of programmed cell death (PCD) initiated upon administration of cytotoxic therapies to tumor cells are often not rigorously defined (3). Considering the growing body of evidence supporting differential immune activation or suppression in response to distinct PCD modalities (4), strategies to maximize the immunogenicity of dying tumor cells could potentially function to boost the effects of co-administered treatments including ICB.

Cells can undergo distinct forms of PCD in response to cellular stress, pathogen infection, and organismal development (5,6). Apoptosis occurs following activation of a family of proteases termed caspases, and the clearance of apoptotic debris is often associated with tolerogenic signaling (7). These immunomodulatory processes include the caspase-directed inactivation of immunostimulatory damage-associated molecular patterns (DAMPs) such as high-mobility group box-1 protein (HMGB1) (8), as well as immunosuppressive functions of the Tyro3/Axl/Mertk receptor tyrosine kinases (TAM RTKs) in promoting tissue repair phenotypes in phagocytes that have engulfed apoptotic debris (9). Notably, apoptosis is believed to be the mechanism of PCD in tumor cells following administration of a wide variety of anti-cancer drugs, including chemotherapeutic agents (10,11), and specific inducers of apoptosis (12–14). Induction of immune tolerance by apoptotic cells may therefore limit synergistic effects when combining these anti-cancer compounds with ICB or other immunotherapy regimens.

Necroptosis is a form of PCD that occurs downstream of the receptor-interacting protein kinases RIPK1 and RIPK3, which assemble into an oligomeric complex termed the 'necrosome' (15,16). A growing body of evidence supports the idea that necroptosis is a more potently immunogenic form of PCD than apoptosis in certain contexts (4). Necroptotic cells undergo rapid membrane permeabilization via the executioner protein mixed-lineage kinase-like (MLKL), leading to the release of intracellular contents including immunogenic DAMPs that can activate innate immune pattern recognition receptors (17–19). Furthermore, death-independent functions of RIPK3 have also been recently defined, including inflammatory chemokine and cytokine production that can promote cross-priming of $CD8^+$ T cell vaccination responses (20) and confer protection during viral infection (21). Therefore, a model emerges in which necroptosis can function as an alternative PCD modality that can eliminate caspase-compromised cells in the event of infection, while simultaneously releasing a payload of inflammatory signals to recruit and activate immune cells (22). Notably, these findings have not yet been comprehensively applied to the field of tumor immunology, in part due to technical limitations related to the manipulation of PCD programs *in vivo*. Indeed, specific targeting of necroptosis using endogenous signaling components is difficult, as there is extensive regulatory cross-talk between extrinsic apoptotic and necroptotic signaling pathways (16). This is further complicated by the fact that many tumors have mutated or silenced either caspases (23) or the RIP kinases (24).

Given these obstacles, the specific differential effects of enforced RIPK3 activation versus caspase-8 or −9 activation within the TME have not been described.

Here, we describe a beneficial role for activation of the necroptotic pathway components RIPK1 and RIPK3 within the TME. Using engineered versions of pro-death enzymes, we present a reductionist system that circumvents endogenous pro-death signaling pathways within tumor cells. Importantly, ectopic activation of RIPK3 promotes tumor antigen loading by tumor APCs associated with enhanced $CD8^+$ leukocyte-mediated anti-tumor responses, which leads to systemic tumor control that synergizes robustly with ICB co-administration. These beneficial effects occur specifically following administration of necroptotic cells within solid tumors, but not following exposure to apoptotic cells or cells dying via lytic necrosis, indicating that these protective effects are due to signals specifically derived from the RIPK1/RIPK3 necrosome complex. We also present a tractable system for the induction of necroptosis in tumor cells *in situ* using engineered AAVs, which successfully recapitulate tumor control effects following necroptosis initiation. Collectively, these findings demonstrate that RIPK1/RIPK3 activation in established solid tumors promotes robust anti-tumor immunity.

Results

Necroptotic cells confer tumor control across multiple syngeneic flank tumor models

To assess the impact of necroptotic tumor cell death on gross tumor outgrowth responses, we utilized a model of intratumoral dying cell administration that allowed us to precisely control the timing and number of cells undergoing various cell death pathways within the TME. We employed constructs encoding chimeric versions of pro-death proteins fused to activatable ("ac") $FKBP^{F36V}$ domains, which we have previously shown allow activation of the chimeric protein following incubation with a synthetic bivalent homologue of rapamycin that functions as a nontoxic ligand (25). Tumor cells transduced with activatable versions of either pro-apoptotic caspase-8 (acCASP8), pro-apoptotic caspase-9 (acCASP9), or pro-necroptotic RIPK3 (acRIPK3) (Figure 1A) were pulsed with ligand drug *in vitro* to enforce oligomerization of these pro-death enzymes, and then injected intratumorally into pre-established syngeneic flank tumors. In this system, ectopically administered cells are alive at the time of injection, but are fated to undergo respective forms of PCD within the TME, accompanied by any signaling activity induced downstream of acCASP8, acCASP9, or acRIPK3. Transduction with pro-apoptotic acCASP9 was better tolerated in tumor cell lines, while acCASP8 was better tolerated in fibroblast cell lines. Using this model, we observed that administration of autologous necroptotic (acRIPK3), but not apoptotic (acCASP9), tumor cells into cell type-matched tumors conferred control of tumor outgrowth and extended survival of animals bearing either B16.F10-OVA melanoma flank tumors (Figure 1B, Figure S1B) or Lewis Lung (LL/2)-OVA adenocarcinoma flank tumors (Figure 1C, Figure S1C).

Unexpectedly, the tumor control effects of necroptosis did not require that necroptotic cells themselves carry tumor antigen, as injection of an unrelated fibroblast line, NIH-3T3, similarly led to tumor control and extension of animal survival following necroptotic, but not apoptotic (acCASP8) fibroblast administration in B16.F10-OVA (Figure 1D, Figure S1D),

LL/2-OVA (Figure 1E, Figure S1E), and E.G7-OVA thymoma (26) (Figure 1F, Figure S1F) flank tumors. These tumor control effects were not an artifact of the immunodominant OVA epitope expressed by tumor cells, as administration of necroptotic fibroblasts also conferred tumor outgrowth and survival extension in mice implanted with non-OVA-expressing B16.F10 (Figure 1G, Figure S1G) or LL/2 (Figure 1H, Figure S1H) flank tumors. These data indicate that necroptotic cells delay tumor outgrowth and even confer complete tumor clearance in a small percentage of animals across multiple syngeneic flank tumor models.

Considering these findings, we next tested if this treatment could act systemically in a bilateral flank tumor model, where a single mouse is implanted with separate B16.F10-OVA tumors on either flank. Following injection of necroptotic fibroblasts into a treated (ipsilateral) tumor, we observed control of flank tumor outgrowth in both the ipsilateral as well as the untreated (contralateral) tumor (Figure 1I), leading to an extension of animal survival and increase in median survival time (Figure 1I). Control of both tumors in this bilateral tumor model indicates an abscopal effect, whereby application of a therapeutic agent to a primary tumor can lead to the control and even elimination of distal, untreated metastases. Notably, this effect required tumor antigen matching between the ipsilateral and contralateral tumors, as mice implanted with a B16.F10-OVA ipsilateral tumor and an antigenically disparate LL/2 contralateral tumor failed to exhibit abscopal tumor control following administration of necroptotic fibroblasts (Figure S1I). These data suggest that the introduction of necroptotic cells to the TME initiates a systemic immune response to tumor-derived antigens, irrespective of antigen matching between necroptotic cells and the tumor cells themselves.

Tumor control by necroptotic cells requires BATF3$^+$ cDC1 and CD8$^+$ leukocytes

Given the unexpected finding that introduction of necroptotic cells to the TME promoted systemic tumor control irrespective of antigen matching, we sought to establish that the control we observed was immune-mediated. BATF3 is a transcription factor required for the development of cDC1 dendritic cells, which are critical for cross-presentation of exogenous antigens to stimulate CD8-mediated immunity, and are required for endogenous anti-tumor immune responses (28). We found that the tumor control effects of necroptotic fibroblasts required BATF3$^+$ cDC1, as *Batf3*$^{-/-}$ mice failed to restrict B16.F10-OVA (Figure 2A) or LL/2-OVA (Figure S2A) tumor growth compared to controls. Consistent with the critical role for cDC1 in mediating anti-tumor immunity, we also observed that depletion of CD8$^+$ leukocytes (including both CD8α$^+$ cytotoxic T cells and CD8α$^+$ dendritic cells) completely abrogated the therapeutic effect of necroptotic fibroblast administration, while depletion of CD4$^+$ leukocytes did not affect tumor control responses (Figure 2B); depletion of each leukocyte population was confirmed via flow cytometry (Figure S2B). These data indicate that control of tumors following introduction of necroptotic cells is immune mediated, and proceeds via activation of CD8$^+$ leukocytes.

Immune-mediated tumor control by necroptotic cells requires NF-κB activation within dying cells, but not DAMP release

We next investigated the signals emanating from necroptotic cells within the TME that promoted immune activation and tumor control. As necroptosis is a lytic form of cell death,

necroptotic cells might initiate immune responses through the release of DAMP molecules within the TME. To assess this possibility, we first tested the ability of necroptotic fibroblasts to recapitulate tumor control effects in several knockout mouse strains, whose tumor-infiltrating immune cells lack expression of pattern recognition receptors (PRRs) capable of recognizing DAMPs, or their downstream signaling components. We found that mice deficient in signaling components involved in cytosolic DNA sensing (*Tmem173*$^{-/-}$, *Mb21d1*$^{-/-}$, *Aim2*$^{-/-}$), cytosolic RNA sensing (*Mavs*$^{-/-}$), TLR signaling (*Myd88*$^{-/-}$, *Ticam1*$^{-/-}$, *Irf3*$^{-/-}$) or general inflammation (*Tnf*$^{-/-}$) all retained the ability to control tumor outgrowth following administration of necroptotic fibroblasts into either B16.F10-OVA (Figure 3A) or LL/2-OVA (Figure S3A) tumors, indicating that the therapeutic effects of necroptotic cells are not strictly mediated through the singular activity of these innate immune signaling components within tumor-infiltrating leukocytes. Furthermore, antibody-mediated blockade of the necrotic cell sensor CLEC9A (29) did not affect tumor restriction or animal survival extension by necroptotic fibroblasts (Figure 3B); effective blockade of CLEC9A expression was confirmed on dendritic cell (DC) subsets in both spleen and tumor (Figure S3B). Taken together, these results indicate that tumor control by necroptotic cells is not mediated solely through the activation of any of these individual innate immune signaling pathways.

Our previous findings indicate that RIPK3 activation induces NF-κB-mediated transcriptional responses in addition to lytic cell death (20). We therefore sought to separate these two potentially immunostimulatory processes to understand the contribution of each to necroptosis-mediated tumor control. To do this, we first administered fibroblasts dying via either necroptosis or lytic necrosis into established B16.F10-OVA tumors, using 3 different forms of lytic necrotic fibroblasts (Figure S1A): (1) cells expressing a mutated version of activatable RIPK3 lacking the RIP Homotypic Interaction Motif (RHIM) domain (acRIPK3ΔC), which cannot recruit and activate RIPK1 to induce downstream NF-κB-mediated inflammatory gene transcription, yet maintains the ability to activate MLKL to induce pore formation and lytic cell death (20); (2) cells expressing an activatable version of MLKL (acMLKL) to induce pore formation and lytic cell death in the absence of upstream RIPK3 activation (30); and (3) cells that were mechanically lysed via repeated freeze/thaw cycles immediately prior to injection. All 3 forms of lytic necrotic cells similarly release cell-associated DAMPs due to loss of plasma membrane integrity, but lack activation of the RIPK1/NF-κB signaling axis that is otherwise observed upon activation of full-length RIPK3 in necroptotic NIH-3T3s (20).

We observed that all 3 treatments of lytic necrotic fibroblasts failed to confer tumor control and extend animal survival compared to fibroblasts dying via acRIPK3-mediated necroptosis, both in single B16.F10-OVA tumors (Figure 3C) and using acRIPK3ΔC fibroblasts in single LL/2-OVA (Figure S3C, left panels) or E.G7-OVA tumors (Figure S3C, right panels). Consistent with this, administration of acRIPKΔC fibroblasts failed to confer tumor control (Figure 3D) and extension of survival (Figure S3D) in bilateral B16.F10-OVA tumor-bearing mice. These results revealed that DAMP release is not sufficient for the tumor control effects of necroptotic fibroblasts within the TME, suggesting instead that signaling activities downstream of RIPK1/RIPK3 necrosome complex formation and activation may play a role.

To more directly test if the immunogenicity of necroptotic fibroblasts in our tumor model depended on intact NF-κB activation in the dying cells, we pre-incubated NIH-3T3 cells +acRIPK3 with an irreversible IκBα phosphorylation inhibitor, BAY-117085, prior to pulsing with activator drug and injection into B16.F10-OVA tumors. Notably, inhibition of NF-κB activation via BAY-117085 significantly reduced both the tumor control effects (Figure 3E) and survival advantage (Figure S3E) conferred by necroptotic cells compared to vehicle-treated controls, indicating that NF-κB activity in necroptotic fibroblasts is required for their anti-tumor effects. To test if the acRIPK3-NF-κB axis was sufficient to drive the tumor control response in the absence of lytic cell death by these cells, we next generated NIH-3T3 cells +acRIPK3 that lacked expression of the necroptosis executioner MLKL (Figure S3F, left panel). These cells failed to undergo cell death upon exposure to activator drug *in vitro*, unless expression of the pro-survival protein cFLIP was concurrently knocked down (Figure S3F, right panel), consistent with reverse-signaling by the RIPK3 complex to induce apoptosis (30, 31). Notably, injection of $MLKL^{-/-}$ NIH-3T3 +acRIPK3 cells into B16.F10-OVA tumors conferred similar tumor control (Figure 3F, left panel) and survival extension (Figure 3F, right panel) responses as seen in mice that received MLKL-sufficient necroptotic fibroblasts. Taken together, these results indicate that transcriptional signaling downstream of RIPK1/RIPK3/NF-κB activation are responsible for the immunogenicity of necroptotic fibroblasts in the TME, and that this occurs independently of DAMP release by dying cells.

Our data point to the production of NF-kB-dependent cytokines as key to tumor control by necroptotic cells. As these cytokines can act both locally and systemically, we next tested whether the introduction of necroptotic cells to the TME might drive systemic inflammatory or immune responses. To do this, we measured levels of inflammatory mediators in sera harvested from B16.F10-OVA tumor-bearing mice following necroptotic cell administration. Notably, there were no differences between treatment groups with respect to systemic levels of inflammatory chemokines and cytokines relevant for anti-tumor responses, including IFN-γ, TNF-α, CCL5, and CXCL10 (Figure 3G), or chemokines and cytokines known to be produced by necroptotic NIH-3T3 fibroblasts, including IL-6, CXCL1, and CCL2 (20) (Figure S3G). Consistent with this, injection of necroptotic fibroblasts into spatially distinct locations distal from the tumor site, including intraperitoneally, intravenously, or subcutaneously on the opposite flank to the tumor, all failed to confer tumor outgrowth control (Figure 3H) or extend animal survival (Figure S3H) compared to intratumoral injection of necroptotic fibroblasts. These data indicate that administration of necroptotic fibroblasts does not lead to tumor control through nonspecific systemic inflammation, suggesting that the therapeutic effect of this treatment is due to local mechanisms exerted specifically within the TME.

Necroptosis promotes anti-tumor $CD8^+$ T cell responses and synergizes with immune checkpoint blockade

We next sought to understand the nature of the immune response instigated by introduction of necroptotic cells to the TME. To do this, we first assessed the effects of dying cell administration on cytotoxic $CD8^+$ T cells, a critical mediator of anti-tumor immunity. Using flow cytometric analysis to identify subsets of OVA-specific (SIINFEKL-$H2K^{b+}$) $CD8^+$ T

cells isolated from B16.F10-OVA tumors (Figure S4A), we observed increased numbers of OVA-specific T cells expressing markers of proliferation ($Ki67^+$), effector function ($GranzymeB^+$), and general activation ($CD44^{hi}$) following necroptotic (acRIPK3), but not apoptotic (acCASP8) or lytic necrotic (acRIPK3ΔC) fibroblast administration (Figure 4A). OVA-specific $CD8^+$ T cells isolated from necroptotic cell-exposed tumor tissue displayed similarly elevated percentages of both $CD44^{hi}$ and $PD\text{-}1^+$ cells (Figure S4B, left and center panels), indicating that necroptosis correlated with an overall more activated surface phenotype of intratumoral $CD8^+$ T cells, though these $CD8^+$ T cells did not express higher levels of PD-1 on a per cell basis compared to cells exposed to apoptotic or lytic necrotic fibroblasts (Figure S4B, right panel). Furthermore, we observed significant increases in the ratios of both activated ($CD44^{hi}$) or tumor-specific (SIINFEKL-$H2k^{b+}$) $CD8^+$ T cells to $CD25^+Foxp3^+$ T_{REG} (Figure 4B) specifically within tumors that received necroptotic fibroblasts, indicating that the profile of tumor-infiltrating T cells was skewed towards more favorable cytotoxic $CD8^+$ T cells, rather than an immunosuppressive profile dominated by T_{REG}. These data indicate that exposure to necroptotic cells within the TME is associated with increased numbers of tumor-specific $CD8^+$ T cells present in the tumor tissue.

In order to characterize the effects of necroptotic cell administration on lymph node priming, we concurrently examined the abundance and quality of $CD8^+$ T cell responses in the tumor-draining lymph node (tdLN) of these mice (Figure S4C). We observed an increased frequency (Figure 4C) and number (Figure S4D) of overall activated (defined as $CD44^{hi}$ $CD62L^{lo}$) $CD8^+$ T cells in the tdLN of mice that received intratumoral necroptotic fibroblasts. These were accompanied by increases in the numbers of bulk $CD8^+$ and single-positive $CD44^{hi}$ $CD8^+$ T cells, but not $CD69^+$ $CD8^+$ T cells (Figure S4D). We also observed similar increases in the frequency (Figure 4D) and number (Figure S4D) of activated, tumor-specific (defined as $CD44^{hi}$ SIINFEKL-$H2k^{b+}$) $CD8^+$ T cells in the tdLN of necroptotic cell-treated mice. Therefore, in addition to an expansion of favorable $CD8^+$ T cell phenotypes locally within the TME, necroptotic fibroblast injection also resulted in lymph node priming of tumor-reactive cytotoxic $CD8^+$ T cells.

To test whether recruitment of these newly-primed $CD8^+$ T cells into the TME was required for necroptotic cells to exert tumor control, we co-administered necroptotic fibroblasts with the sphingosine-1-phosphate receptor modulator FTY-720 to inhibit egress of lymphocytes from the tdLN. Interestingly, blockade of lymphocyte trafficking did not affect B16.F10-OVA tumor control by necroptotic fibroblasts, as FTY-720-treated animals still exhibited effective control over tumor outgrowth and extension of animal survival compared to vehicle-treated controls (Figure 4E). Consistent with a lack of influx of newly-primed lymphocytes, enumeration of various tumor-associated lymphocyte populations isolated from B16.F10-OVA tumors 48 hours post-dying cell administration revealed similar total numbers of $CD19^+$ B cells, $CD4^+$ T cells, and $CD8^+$ T cells within the TME among tumors that received apoptotic (acCASP8), necroptotic (acRIPK3), or lytic necrotic (acRIPK3ΔC) cell injections (Figure S4E).

Notably, inhibition of lymph node egress by primed leukocytes also did not alter abscopal tumor control in bilateral B16.F10-OVA tumors (Figure 4F, S4F), suggesting that untreated contralateral tumor control could be mediated by re-circulating leukocytes in the periphery.

These results show that rapid recruitment of tumor-reactive lymphocytes from the tumor-draining lymph node is not required for growth restriction of treated or distal, untreated tumors responding to necroptotic fibroblast exposure, and further implicate local effects of necroptotic cells within the TME.

The efficacy of ICB is often boosted upon co-administration with cytotoxic therapies, including irradiation (2). Because stimuli from necroptotic cells boosted activation of tumor-specific $CD8^+$ T cells both in tumor and in tumor-draining lymph node, we hypothesized that the presence of necroptotic cells within the TME that would synergize with ICB, specifically α-PD-1. To test this, we interleaved injections of necroptotic fibroblasts into B16.F10-OVA flank tumors with administration of α-PD-1, and observed that mice exhibited significantly improved survival outcomes (Figure 4G) and improved tumor growth restriction (Figure S4G, left panel), as 71.4% of mice successfully cleared their tumors (Figure S4G, right panel) following this co-administration regimen. To determine whether this successful combination therapy conferred protective immune memory, we re-challenged mice ~2 months after they successfully cleared their tumors, injecting identical tumor cells into the same flank that bore the initial B16.F10-OVA tumor (Figure 4H, left panel). Notably, 100% of mice were protected from tumor re-challenge (Figure S4H) and failed to succumb to tumor outgrowth compared to naïve B6/J controls (Figure 4H, right panel). Altogether, these data indicate that necroptosis in the TME can potently synergize with ICB co-administration to promote durable tumor rejection.

Exposure to necroptosis in the TME promotes antigen uptake and activation of tumor-associated APCs

Our data indicate that necroptosis potentiates anti-tumor $CD8^+$ T cell responses even when necroptotic cells do not contain tumor antigen, implicating broad activation of tumor-associated antigen-presenting cells as the key effect of necroptotic cells within the TME. We therefore aimed to define necroptosis-induced changes to tumor-associated myeloid cell populations that could function to initiate adaptive immunity. Using a previously published gating strategy to identify subsets of tumor-associated innate immune cells (Figure S5C) (32), we enumerated various innate immune cells isolated from B16.F10-OVA tumor tissue following administration of apoptotic (acCASP8), lytic necrotic (acRIPK3ΔC), or necroptotic (acRIPK3) fibroblasts. Notably, we observed a significant increase in the number of $CD24^+$ $CD103^+$ DC1 (Figure 5A), although there were no significant differences in the number of $Ly6C^{hi}$ monocytes, $NK1.1^+$ NK cells, bulk $MHCII^+$ antigen-presenting cells (APCs), $F4/80^+$ macrophages, or $CD24^+$ $CD11b^+$ DC2 (Figure 5A, Figure S5A). This was promising, given that $CD103^+$ DC1 are often viewed as the most functional tumor APC subset with respect to stimulating $CD8^+$ T cell-mediated anti-tumor immunity (27, 32–33). Consistent with this increase in intratumoral $CD103^+$ DC1, we measured significantly elevated levels of the DC chemoattractants CCL3, CCL4, and CCL5 in tumor homogenates following exposure to necroptotic fibroblasts (Figure 5B). Considering that $CD103^+$ DC1 can be recruited to the TME via NK cell-derived chemokines (34), we tested whether depletion of NK cells (Figure S5B, right panel) abrogated the therapeutic effect of necroptotic fibroblasts. Interestingly, NK cell depletion had no effect on tumor control and survival extension (Figure S5B, left panel) by necroptotic fibroblasts.

We next evaluated the phenotype of phagocytic tumor APCs with respect to tumor antigen loading and their activation status. To do this, we implanted mice with B16.F10-OVA cells that also express the bright and stable fluorophore zsGreen, then gated on zsGreen$^+$ tumor-associated phagocytes to identify tumor APCs that have ingested tumor-derived material (Figure 5C, Figure S5C). Using this gating strategy, we identified zsGreen$^+$ subsets of 6 primary tumor APC populations: bulk CD24$^+$ DCs, CD103$^+$ DC1, CD11b$^+$ DC2, bulk F4/80$^+$ tumor-associated macrophages (TAM), CD11b$^+$ TAM1, and CD11c$^+$ TAM2. Intriguingly, the proportion of zsGreen$^+$ cells was significantly increased across all tumor APC subsets following administration of non-zsGreen-labeled necroptotic fibroblasts; this increase was particularly pronounced in the DC subsets examined (Figure 5D). Accordingly, the absolute number of zsGreen$^+$ cells among tumor DC subsets was increased following necroptotic cell exposure (Figure S5D). As zsGreen expression was restricted to B16.F10-OVA tumor cells in this model, these results show that signals derived from necroptotic fibroblasts act *in trans* to increase either the rate of phagocytosis or the retention of tumor-associated antigen within tumor APC populations.

To further characterize the phenotype of tumor APCs in our model, we evaluated expression of the necrotic cell uptake marker CLEC9A on DCs, and inhibitory PD-L1 on tumor cells and across different APC subsets. Exposure to necroptotic fibroblasts changed neither cell surface expression of either CLEC9A (Figure 5E) or PD-L1 (Figure 5F), nor the percentage of CLEC9A$^+$ (Figure S5E) or PD-L1$^+$ (Figure S5F) populations from each cell subset. We also assessed the activation status of zsGreen$^+$ tumor APCs following exposure to dying fibroblasts within the TME. We first observed that zsGreen$^+$ tumor APCs expressed higher levels of the costimulatory marker CD80 on a per cell basis following administration of necroptotic fibroblasts; this increase was consistent across all 6 tumor APC subsets examined (Figure 5G). Notably, we also observed a significant increase in the gMFI of CD80 following exposure to necroptotic cells when gating on zsGreen$^-$ (non-tumor antigen-loaded) populations of each tumor APC subset (Figure S5G), revealing that stimuli derived from necroptotic fibroblasts increased CD80 expression across all tumor APCs, regardless of tumor antigen uptake status. Importantly, this increase in activation marker expression correlated with an improved functional capacity of zsGreen$^+$ tumor APCs following exposure to necroptotic cells in the TME, as zsGreen$^+$ tumor APCs sorted *ex vivo* were capable of more robustly stimulating proliferation of previously-activated transgenic OVA-specific (OT-I) CD8$^+$ T cells in an *in vitro* co-culture system (Figure 5H). This stimulatory effect was limited to CD8$^+$ T cells with TCR specificity for tumor antigen, as *ex vivo* co-culture of zsGreen$^+$ tumor APCs did not induce proliferation of T cells expressing an irrelevant LCMV GP33 TCR (P14 transgenic TCR, Figure S5H). Therefore, exposure to necroptotic cells in the TME increases not only the abundance, but also the immunostimulatory quality of tumor antigen-loaded tumor APCs.

Consistent with this, we found that necroptotic cells appear to enhance antigen uptake by phagocytes in a tumor-independent setting, as co-culturing bone marrow-derived macrophages (BMDMs) with necroptotic B16.F10 tumor cells *in vitro* resulted in increased uptake of an inert dextran-fluorophore substrate included in the co-culture, compared to BMDMs cultured with live B16.F10 cells (Figure 5I, left panel). Notably, uptake of this bystander substrate was also associated with an increase in CD80 expression on both dextran

$^{+}$ and zsGreen^{+} BMDMs only following co-culture with necroptotic B16.F10 cells (Figure 5I, center and right panels), while expression of the immunomodulatory markers CD206 and VCAM-1 was decreased on zsGreen^{+} BMDMs co-cultured with necroptotic tumor cells compared to live tumor cell controls (Figure S5I). Collectively, these data indicate that stimuli derived from necroptotic cells increase antigen loading by phagocytic cell subsets, and that this effect may constitute a conserved response to necroptotic cell-derived stimuli rather than a tissue-specific effect restricted to the TME.

Engineered adeno-associated viruses (AAVs) can be used to specifically induce necroptosis of tumor cells *in vitro*

Intratumoral dying cell injection provides a cleanly controlled model for examining how exposure to stimuli derived from necroptotic cells can influence anti-tumor immune responses. However, an obvious caveat of this model is that it fails to assess immune responses to tumor cell necroptosis *in situ*. To address this, we sought to create reagents that would allow direct induction of necroptosis in tumors *in vivo*. To achieve this, we generated versions of RIPK3 fused to a constitutively-oligomerizing ("co") domain, which consists of a high-affinity 2L6HC3-9 homotrimerizing domain that has been previously synthesized and described (35). These chimeric forms of RIPK3 undergo oligomerization and activation upon their expression in cells, independent of any upstream signaling or the presence of a ligand. To deliver these reagents to tumor cells, we created AAVs containing genes encoding these constructs under control of a synthetic MND (myeloproliferative sarcoma virus enhancer, negative control region deleted, *d*l587rev primer-binding site substituted) promoter, enabling robust gene expression in target cells. Upon transduction of a target cell by these engineered AAVs, the chimeric pro-death protein of interest is expressed, constitutively oligomerizes, and leads to rapid and specific induction of RIPK3-dependent cell death (Figure 6A, Figure S6A).

AAVs are a flexible tool for primary cell transduction, as several serotypes with varying cellular tropisms have been described. We therefore sought to identify an AAV serotype that would selectively deliver construct expression to B16.F10 melanoma cells. Using a hybrid AAV2.5 serotype (36), we observed robust transduction of cultured B16.F10 tumor cells within 24 hours of eGFP-AAV2.5 (eGFP) addition (Figure 6B). Importantly, the AAV2.5 serotype also transduced non-leukocytic CD45^{-} cells within B16.F10-OVA tumors *in vivo*, exhibiting successful eGFP transduction in a higher percentage of CD45^{-} cells compared to AAV5, AAV6, AAV8, or AAV9 serotypes (Figure S6B). eGFP-AAV2.5 also had the lowest percentage of off-target transduction of CD45^{+} tumor-associated leukocytes *in vivo* (Figure S6B). We therefore concluded that the hybrid AAV2.5 serotype would maximize tumor cell transduction efficiency while limiting off-target transduction of immune cells when adapted for use *in vivo*, potentially limiting off-target toxicity effects.

Next, we characterized the kinetics of death induced by AAV2.5 particles that deliver genes encoding chimeric pro-death proteins *in vitro*. Transduction of B16.F10 tumor cells with necroptosis-targeting AAV2.5 (coRIPK3) or lytic necrosis-targeting AAV2.5 (coRIPK3ΔC) led to 100% cell death within ~15 hours (Figure 6C). Consistent with induction of necroptosis by these reagents, we found that the pan-caspase inhibitor zVAD-fmk did not

affect death induction by coRIPK3 or coRIPK3ΔC (Figure S6C, left panel), while addition of the RIPK3 inhibitor GSK-843 eliminated coRIPK3ΔC-induced death while decreasing coRIPK3-induced death; this latter effect was likely due to reverse signaling through the RIPK1/RIPK3 necrosome to induce apoptosis, as previously described (Figure S6C, center panel) (30,31). Consistent with this, incubation with both zVAD-fmk and GSK-843 eliminated all cell death associated with coRIPK3 treatment (Figure S6C, right panel). This set of experiments shows that either necroptosis or lytic necrosis can be specifically and rapidly induced in B16.F10 tumor cells *in vitro* upon AAV-mediated delivery of coRIPK3 or coRIPK3ΔC, respectively.

As our data using fibroblast injection pointed to activation of NF-κB responses by RIPK3, but not RIPK3ΔC, as a key mediator of anti-tumor immune responses, we next assessed the ability of our AAV constructs to activate inflammatory transcription in dying cells. To do this, we infected B16.F10 tumor cells *in vitro* with AAVs encoding coRIPK3 or coRIPK3ΔC for 10 hours (a time point at which tumor cells have not yet undergone membrane permeabilization, allowing for nucleic acid isolation) and then harvested total RNA for Nanostring analysis. Transduction of tumor cells with coRIPK3 yielded a distinct transcriptional signature compared to cells transduced with coRIPK3ΔC (Figure S6D). Further examination of this signature revealed that necroptotic B16.F10 cells exhibited upregulated expression of numerous NF-κB-dependent gene targets, including *Lta, Ltb, Cd40, Cd86, Mef2a Nod2*, and *Nos2* in comparison to lytic necrotic tumor cells (Figure 6D). Additionally, necroptotic B16.F10 cells also upregulated expression of several inflammatory chemokines and cytokines, including *Cxcl1, Cxcl3, Ccl2, Ccl3, Ccl4, Ccl21a, Ccl22, Il12b, Il22*, and *Ifng* (Figure 6D). Upregulated transcript levels for several of these target genes were independently validated via qRT-PCR (Figure S6E). Taken together, these data indicate that the induction of tumor cell death via coRIPK3 transduction *in vitro* leads to an inflammatory transcriptional signature consistent with immunogenic necroptosis (20). Furthermore, this gene signature depends on the assembly of the RIPK1/RIPK3 necrosome via RHIM-RHIM interactions, as it is absent in tumor cells transduced with coRIPK3ΔC.

Administration of necroptosis-targeting AAVs in conjunction with α-PD-1 *in vivo* promotes durable tumor clearance

Following validation of our PCD-targeting AAVs *in vitro*, we applied these tools to study anti-tumor responses *in vivo*. Intratumoral administration of coRIPK3 conferred control of B16.F10-OVA tumor outgrowth (Figure 7A) and extension of animal survival (Figure S7A) in comparison to intratumoral injection of coRIPK3ΔC or control eGFP. Analysis of tumor homogenates revealed increased concentrations of numerous beneficial anti-tumor cytokines and chemokines following coRIPK3 administration, including IFN-γ, CCL3, CCL5, and CXCL10 (Figure 7B), while levels of IL-6, CXCL1, and CXCL2 were unchanged (Figure S7B). Furthermore, we observed abscopal tumor control effects in a bilateral B16.F10-OVA flank tumor model, as coRIPK3 administration conferred control over tumor outgrowth in both treated (ipsilateral) and untreated (contralateral) tumors (Figure 7C) and significantly extended animal survival (Figure S7C). These results recapitulate the tumor control effects that we observed in a bilateral tumor model using necroptotic fibroblast administration,

showing that enforced RIPK3 activation via AAVs can similarly promote tumor control that is associated with increased intratumoral levels of inflammatory chemokines and cytokines.

Next, we tested if necroptosis-targeting AAVs could similarly protect mice from single B16.F10-OVA tumor outgrowth upon co-administration with α-PD-1. Not only did administration of coRIPK3 with isotype controls significantly extend animal survival (Figure 7D) and inhibit tumor growth (Figure S7D) in comparison to eGFP-treated control mice, but the co-administration of coRIPK3 with α-PD-1 led to robust responses, with improved overall survival (Figure 7E) complete tumor clearance in 69.2% of mice (Figure S7E, right panel) and significant control over tumor outgrowth (Figure S7E, left panel). Again, these tumor elimination responses closely paralleled those observed in the intratumoral necroptotic fibroblast injection model.

B16.F10-OVA tumor control following co-administration of coRIPK3 + isotype or α-PD-1 required the presence of $CD8^+$ leukocytes, as depletion of $CD8^+$ cell subsets via antibody injection completely abrogated the protective effects of coRIPK3 + IgG2a or α-PD-1 (Figure 7F, Figure S7F). Additionally, mice lacking $BATF3^+$ cDC1 also failed to control B16.F10-OVA tumors following coRIPK3 + α-PD-1 treatment regimen (Figure 7G, Figure S7G). Considering that tumor control by necroptotic fibroblasts also necessitated the presence of these immune cell compartments, these experiments revealed similar effector cell subset requirements between both intratumoral dying fibroblast and intratumoral AAV models. With these requirements in mind, we next sought to test if the mice that had successfully cleared their B16.F10-OVA tumors following dual therapy (Figure 7E) had developed protective immune memory. To this end, we re-challenged surviving animals with identical tumor cells on the same flank that initially bore the B16.F10-OVA tumors (Figure 7H, left panel). Strikingly, the majority of these animals were protected from mortality due to tumor outgrowth (Figure 7H, right panel), as only 12.5% of mice regrew tumors (Figure S7H) compared to 100% of naïve controls. Overall, these data demonstrate that intratumoral administration of necroptosis-targeting AAVs in conjunction with α-PD-1 confers durable, immune-mediated tumor rejection similar to that observed upon administration of intratumoral necroptotic NIH-3T3 fibroblasts.

AAV-mediated transduction of tumor cells allows for enforced expression of activated RIPK3, regardless of the expression status of endogenous RIPK3. Considering the beneficial effects of enforced RIPK3 activation that we observed in our murine melanoma model, we asked how endogenous levels of RIPK3 correlated with survival outcomes in human cancer patients. Using tumor biopsy RNAseq data available through The Cancer Genome Atlas (TCGA) database, we stratified human skin cutaneous melanoma patients based on upper (High) and lower quartiles (Low) of RIPK3 transcript expression within the tumor tissue. Strikingly, patients with high tumor RIPK3 expression exhibited significantly improved survival outcomes compared to low RIPK3-expressing patients (Figure 7I). Furthermore, multivariate Cox regression modeling revealed a negative coefficient (−0.175), indicating that high expression of RIPK3 is correlated with a better survival outcome (Figure 7I) (37). Altogether, these results show that higher levels of RIPK3 expression within melanoma tumors are associated with improved survival in a subset of human patients.

Discussion

Distinct forms of PCD can differentially instruct subsequent immune responses mounted against antigens derived from dying cells. Here, we describe a role for RIPK1/RIPK3 activation in which necroptotic fibroblasts within the TME drive increased antigen uptake and activation of tumor APCs to potentiate tumor-specific $CD8^+$ T cell immunity, which synergizes with α-PD-1 co-administration to confer durable tumor rejection (Figure 8). These gross tumor control effects are recapitulated in a model of AAV-mediated induction of necroptosis within melanoma tumor cells *in situ*, indicating that enforced activation of RIPK3 may lead to beneficial inflammatory signaling that is conserved across multiple cell types. Importantly, our data indicate that tumor control by necroptotic cells is primarily mediated via the activation of a RIPK1/RIPK3/NF-κB signaling axis independently of cell lysis, as MLKL deficiency in fibroblasts does not abrogate tumor control (Figure 3F), while NF-κB inhibition or use of a mutant form of RIPK3 that triggers cell lysis without engaging RIPK1-dependent transcription eliminates the therapeutic efficacy of these cells (Figure 3E). Thus, while in most experiments reported here we are engaging necroptotic cell death (as defined by activation of MLKL by RIPK3), activation of transcription that parallels cell death is likely the cause of the beneficial immune stimulation we observe. These findings join a growing number of reports of biological effects of RIPK1/RIPK3 signaling that are independent of MLKL activation (21, 38–41).

Existing therapies to target RIPK1/RIPK3 activation *in vivo* exhibit variable efficacy due to off-target effects of global caspase inhibition (42) and the differential expression status of endogenous RIPK3 in tumor cells (23,24). AAV-mediated reconstitution of constitutively active RIPK3 within tumor cells represents a novel strategy to specifically induce this pathway independently of any endogenous signaling requirements. Another group recently reported that intratumoral delivery of mRNA encoding MLKL to promote cell lysis *in situ* conferred protection in murine melanoma and colon carcinoma models (43), and while our findings diverge from theirs with regard to a requirement for NF-kB signaling within dying cells, both studies support the idea that reconstituting expression of necroptotic signaling components can promote anti-tumor immunity. Considering that high levels of RIPK3 expression in human melanoma tumors correlate with improved patient survival (Figure 7I), we propose that such strategies to restore or increase necroptotic signaling in human tumors represent a promising therapeutic target in future translational research.

Future work will need to define the specific signals derived from necroptotic cells that are responsible for mediating our observed anti-tumor immune responses. Across both dying cell and AAV administration models, the therapeutic effects of necroptotic cells appear to occur independently of MLKL activation, cell lysis, and subsequent DAMP release, and suggest that NF-κB transcriptional signaling downstream of the RIPK1/RIPK3 necrosome complex is required for therapeutic efficacy of necroptosis in the TME. Interestingly, our observation of increased tumor-derived antigen within tumor APCs exposed to necroptotic cells is consistent with a previous report of necrotic debris being ingested alongside extracellular contents via macropinocytosis (44). However, the specific signals derived from necroptotic cells that are responsible for driving macropinocytosis to increase sampling of the local extracellular microenvironment remain unknown; our data imply that these signals

are defined by cytokines, rather than DAMPs, produced by dying cells. Defining the mechanistic targets of RIPK1/RIPK3 activation and how these targets interact with tumor APCs to drive either increased macropinocytosis or improved retention of tumor antigen in order to better stimulate cytotoxic $CD8^+$ T cells remains an important area for future study.

The overarching goal of tumor immunotherapy is to engage cytotoxic $CD8^+$ T cells to kill tumor cells. This branch of the immune response evolved to combat intracellular pathogens such as viruses; treatments that activate innate immune pathways associated with viral sensing within tumors have therefore proven effective at provoking cytotoxic anti-tumor immunity. Such approaches include agonism of nucleic acid sensing via cGAS/STING (45,46) and TLR pathways (47). The necroptotic pathway likely evolved to combat viral infection via elimination of the replicative niche, and is also promotes cross-priming of the $CD8^+$ T cell responses required for viral elimination (20). Activation of this pathway within tumors can therefore be considered an additional strategy to direct anti-viral immunity toward tumor elimination. While much work remains to validate these findings in clinically relevant models, our data suggest that RIPK1/RIPK3 activation within the TME warrants further development as a component of tumor immunotherapy.

Materials and Methods

Study design

Pilot studies were used to estimate mean differences in tumor growth between treatment groups. Using the Sample Size Calculator resource (Boston University), we calculated biological replicate numbers needed to avoid experimental underpowering by using the percent difference in group means from pilot studies, with 0.80 power level and α level = 0.05. Age-matched mice were randomly assigned to treatment groups, and tumor measurements were conducted by a researcher blinded to treatment groups for at least 1 experimental replicate.

Cell culture

B16.F10-OVA, LL/2-OVA, NIH-3T3, and HEK-293T cells were maintained in Dulbecco's modification of Eagle medium (DMEM) supplemented with 10% (vol/vol) FBS, 2mM L-glutamine, 10mM HEPES, and 1mM sodium pyruvate (complete DMEM). E.G7-OVA cells were maintained in RPMI 1640 supplemented with 10% FBS, 2mM L-glutamine, 10mM HEPES, 1mM sodium pyruvate, 0.05mM beta-mercapthoethanol, 0.4mg/mL geneticin (G418), and 4.5g/L D-glucose. B16.F10 and LL/2 cell lines were transduced with a plasmid (pSLIK) encoding activatable versions of caspase-9 or RIPK3 under TRE control; thus, these cells were cultured in 1μg/mL doxycycline (Sigma) for 18h to induce construct expression prior to harvesting as described below for dying cell injections. Bone marrow-derived macrophages (BMDMs) were cultured in complete DMEM + penicillin/streptomycin + 20ng/mL rM-CSF and differentiated for 7 days prior to plating for experiments. All cells were cultured at 37°C with 5% CO_2.

Mice

C57BL6/J (B6/J) mice were purchased (Jackson) and allowed to acclimate up to one week prior to experiment initiation. All other genotypes were bred and housed under specific-pathogen-free conditions at the University of Washington. All animals were maintained according to protocols approved by the University of Washington Institutional Animal Care and Use Committee (IACUC).

Tumor models

6–10 week old female (B16.F10-OVA, E.G7-OVA) or male (LL/2-OVA) mice were injected subcutaneously on the right flank with 1×10^5 (B16.F10-OVA, E.G7-OVA) or 2×10^5 (LL/2-OVA) tumor cells, mixed in a 1:1 volumetric ratio with the basement membrane matrix Matrigel HC (Corning) for a final injection volume of 100μL. For bilateral tumor experiments, mice were equivalently implanted with tumor cells on the left flank on the same day (d.0) of right flank tumor injection. As previously described (45), tumor volume was calculated using the following formula: Volume = Short axis^2 × Long axis × 0.523. Mice were euthanized once tumor burden reached a volume ≥2000mm^3. Mice that developed skin ulceration over the tumor site were excluded from experimental analyses. Complete tumor clearance was determined by the absence of a palpable tumor mass at the site of tumor injection.

Intratumoral dying cell injections

NIH-3T3, B16.F10, or LL/2 cells stably transduced with pro-death constructs were harvested activated as previously described (20). Briefly, 5×10^6 cells/mL were incubated in complete DMEM + 1mM of B/B homodimerizer (Clontech) for 15min at 37°C. Cells were then washed with cold PBS, resuspended at 20×10^6 cells/mL, and kept on ice prior to injection. 1×10^6 dying cells were administered intratumorally in 50μL. Remaining cells were re-plated and cultured at 37°C overnight to ensure <95% of treated cells underwent PCD. Dying cells were administered on days 6, 8, and 10 post-initial tumor challenge. For experiments involving IκBα inhibition, NIH-3T3 cells were pre-treated with 10μM BAY 11–7085 (Cayman Chemical) for 45min prior to harvesting for B/B homodimerizer incubation, as described (20).

In vivo antibody administration

200μg of α-CD8 (clone 2.43, BioXCell), α-CD4 (clone GK1.5, BioXCell), α-PD-1 (clone RMP1–14, BioXCell), or respective isotype controls were administered to mice via intraperitoneal injection on days 5, 7, 9, and 11 post-initial tumor challenge. NK cell depletion experiments followed the same dosing protocol, using 250μg of α-NK1.1 (clone PK136, BioXCell). CLEC9A blocking experiments followed the same dosing protocol, using 400μg of α-CLEC9A (clone 7H11, BioXCell) or isotype control, as described (28).

Recombinant AAV cloning

Design and sequencing analysis of all plasmids was performed using Geneious software v. 7.1 (48). The 2L6HC3-13 trimer homo-oligomer domain was a gift from Dr. David Baker (35). Trimerizing RIPK3 constructs were directly cloned into a single-stranded AAV

(ssAAV) vector using multi-fragment assembly (Infusion HD, Takara Biosciences). AAV backbone was linearized using SnaBI digest as previously described (49). Primers for amplification of gene fragments were designed to contain 20 base pair 5' and 3' homology to neighboring fusion sequences, and PCR amplification was carried out using Q5 Polymerase (New England Biosciences). The shortened 3' UTR WPRE and polyA elements were amplified from pAAV-CW3SL-EGFP, a gift from Bong-Kiun Kaang (Addgene #61463). Sense and anti-sense primer sequences were as follows: Fragment 1 (MND Promoter): (S) CCGCCATGCTACTTATCTACGGAGTCGTGACCTAGGGAACAGAGAAACAGG, (AS) TTCGAGGAAGTCAAAACAGCGTGG;

Fragment 2 (RIPK3 and RIPK3ΔC): (S) CGCTGTTTTGACTTCCTCGAACCATGTCTTCTGTCAAGTTATGG, (full length RIPK3 AS) AGAACCACTCCCTTCTGATCCTTCGGAACCCGTACGCTTGTGGAAGGGCTGCCAGC, (RIPK3ΔC AS) AGAACCACTCCCTTCTGATCCTTCGGAACCCGTACGTCATTGGATTCGGTGGGGTC; Fragment 3 (2L6HC3-13 homo-trimer domain): (S) GATCAGAAGGGAGTGGTTCTCATATGGGTACGAAATACG, (AS) CAGAGGTTGATTATGCGGCCTTAGTCACTTTTGGCGTTAATTTTC;

Fragment 4 (sWPRE/polyA): (S) GGCCGCATAATCAACCTCTGG, (AS) CCGCCATGCTACTTATCTACAAAAAACCTCCCACATCTCCCCC.

The MND-eGFP self-complementary AAV (scAAV) was a gift from Dr. David Rawlings. The DNA sequence of inserted elements was verified by sequencing, and the integrity of the viral inverted terminal repeat (ITR) within the pAAV backbone confirmed by restriction digest using AhdI, BglI or SmaI, prior to viral production.

Adeno-associated virus (AAV) production, purification, and quantification

AAVs were produced as described (50,51). Briefly, AAV stocks were generated in HEK293T cells via PEI transfection using vector + serotype helper (pLTAAV). Cells were harvested 48h post-transfection, lysed via freeze/thaw cycling, treated with 100U/mL Universal Nuclease (Thermo) at 37°C for 30 minutes, and purified via centrifugation over an iodixanol density step gradient. Titers of viral stocks were determined via qRT-PCR analysis in conjunction with TaqMan reagents and a ViiA 7 Real-Time PCR apparatus (Applied Biosystems). qRT-PCR for viral titer used primers targeting the conserved ITR, using the following sequences: (F) GGAACCCCTAGTGATGGAGTT, (R) CGGCCTCAGTGAGCGA.

Intratumoral AAV injections

1×10^{11} infectious units (IFU) of respective AAV were administered intratumorally in 50μL. Virus aliquots used for *in vivo* experiments were thawed once following initial freezing post-purification. AAV injections were administered on days 6, 8, and 10 post-initial tumor challenge.

Flow cytometry and cell sorting

Leukocytes were isolated from either tumor-adjacent inguinal lymph node (iLN) or spleen by mashing over a 70μM strainer, or from tumor tissue by digesting minced tumors in 1× PBS + 2.6mg/mL Collagenase A (Sigma) + 23U/mL DNase I (Sigma) at 37°C with agitation for 45min prior to mashing tissue over a 70μM strainer. 1–3 × 10^6 cells were blocked with anti-CD16/32 (BD Biosciences) and stained with Zombie viability dye (BioLegend) at room temperature for 30min. Cells were then incubated with appropriate fluorochrome-conjugated antibodies in 1× PBS + 0.5% FBS + 2mM EDTA at for 4°C for 1h. Permeabilization and intranuclear staining were performed using a Foxp3 Intranuclear Transcription Factor Staining Kit (eBiosciences). Data were collected using an LSRII flow cytometer (BD) and analyzed using FlowJo software (Treestar). For sorting of zsGreen$^+$ tumor APC populations, B16.F10-OVA-zsGreen tumors were harvested 48h post-intratumoral dying cell injection, leukocytes were processed and stained as described above, and subsets were sorted using a FACSAria II (BD).

OT-I/P14 proliferation assay

Lymph nodes and spleens from OT-I or P14 TCR transgenic mice were processed and enriched for CD8$^+$ T cells via negative selection using biotinylated antibodies against B220, CD4, CD11b, CD11c, and Ter119 (eBioscience) followed by magnetic separation. Purified transgenic T cells were activated via 6 day co-culture with irradiated splenocytes pulsed with 100ng/mL SL8 (for OT-I) or GP33 (for P14) peptides (Invivogen). 20,000 previously-activated transgenic T cells were labeled with 5μM CellTrace Violet (Thermo Fisher) and plated with 4,000 sorted zsGreen$^+$ tumor APC subsets in 96 well U-bottom plates for 72h prior to analysis of proliferation dye dilution via flow cytometry.

Murine cytokine assessment

To evaluate serum cytokine levels, sera were harvested from mice receiving indicated intratumoral treatments 48h post-dying cell administration and stored for <2 weeks at −80°C. As a positive control for systemic inflammation, B6/J mice were injected intraperitoneally with 40mg/kg of the STING agonist DMXAA (ApexBio), and sera were harvested 5h post-injection, then frozen at −80°C. To evaluate intratumoral cytokine levels, tumors were harvested 48h post-dying cell administration or 72h post-AAV administration. Tumors were then minced and homogenized using metal beads with vigorous shaking in tubes, then frozen at −80°C. To evaluate cytokine levels *in vitro*, 3 × 10^5 B16.F10 cells were infected with 1 × 10^{11} IFU of AAV for 18h, and supernatants were frozen at −80°C. Thawed samples were analyzed using a Th1/Th2 ProcartaPlex™ Panel 1 Luminex kit (Thermo Fisher).

Nanostring RNA analysis and qRT-PCR

2 × 10^6 B16.F10 cells were infected with 1 × 10^{11} IFU of respective AAV for 10h. Total RNA was isolated using a Nucleospin RNA Kit (Macherey-Nagel) and run on an nCounter Sprint in conjunction with an nCounter Mouse Inflammation V2 Panel (Nanostring). Data were normalized and analyzed using nSolver software (Nanostring). For target gene validation, oligo(dT) random hexamers and SuperScript III Reverse Transcriptase (Life

Technologies) were used to synthesize cDNA from the same total RNA samples used for Nanostring analysis. Fluorogenic quantitative reverse transcriptase PCR (qRT-PCR) analysis was performed using previously published oligonucleotide primer sequences using SYBR Green reagents and a ViiA 7 Real-Time PCR apparatus (Applied Biosystems). Cycle threshold (CT) values for target genes were normalized to CT values of the housekeeping gene *Gapdh* ($\Delta CT = CT_{Target} - CT_{Gapdh}$), and subsequently normalized to baseline control values ($\Delta\Delta CT = \Delta CT_{Experimental} - \Delta CT_{Control}$).

In vitro cell death assay

1×10^5 B16.F10-OVA cells were infected with 1×10^{11} IFU of respective AAV in 24 well plates for 24h. Cell viability was evaluated via incorporation of cell viability dye Sytox Green (Molecular Probes) or Yoyo-3 (200nM, Life Technologies) and quantified using a 2-color Incucyte Zoom bioimaging platform (Essen Biosciences), as described (52). Where indicated, 50μM zVAD-fmk (SM Biochemicals) or 100nM GSK-873 (GlaxoSmithKline) were added to inhibit pan-caspase activation or RIPK3 activation, respectively.

CRISPR/Cas9 gene targeting

The following guide RNA (gRNA) sequences were cloned into a pRRL-Cas9-T2A-puromycin CRISPR/Cas9 lentiviral vector (a gift from Dr. Daniel Stetson (53)): murine non-targeting gRNA (5'- GCGAGGTATTCGGCTCCGCG −3')(54); murine *Mlkl* gRNA (5'-GCACACGGTTTCCTAGACGC −3'). Constructs were transduced into NIH-3T3 +acRIPK3 cells using standard lentiviral transduction protocols, and selected in 1μg/mL puromycin.

siRNA knockdown

2×10^5 $MLKL^{-/-}$ NIH-3T3 cells +acRIPK3 were transfected with SiGenome SMARTpool siRNAs (Dharmacon) targeting murine RIPK1 (M-040150–01), murine caspase-8 (M-043044-01), murine cFLIP (M-041091-01), or non-targeted "scramble" pool (D-001206-14), using Lipofectamine siRNA Max (Life Technologies). 48h post-transfection, cells were re-plated, treated with 100nM B/B homodimerizer (Clontech), and cell death kinetics were characterized as described above.

Western blot

Cell lysates were harvested and quantitated using a BCA Protein Assay (Thermo). 30μg total protein/sample were separated using SDS-PAGE gels (Invitrogen) and detected using traditional protocols. The following antibodies were used for protein detection: rat α-MLKL clone 3H1 (EMD Millipore), rabbit α-FKBP12 (Thermo), mouse α-actin C4 (EMD Millipore), goat α-rat IgG-HRP (Santa Cruz), donkey α-rabbit IgG-HRP (Santa Cruz), and goat α-mouse IgG-HRP (Santa Cruz).

In vitro dextran uptake assay

BMDMs were plated in a 1:5 ratio with either live or acRIPK3-expressing B16.F10-zsGreen tumor cells. acRIPK3 cells were induced to die upon 18h incubation with 1μg/mL doxycycline prior to co-culture with BMDMs, then incubated with 100nM B/B homodimerizer (Clontech) for 24h before adding 1mg/mL Dextran-PE.TexasRed (10,000

MW, Thermo Scientific). Dextran incubations were performed in triplicate at either 4°C or 37°C for 30min, and plates were tapped every 10min to mix. Cells were washed 3×, stained with fluorochrome-conjugated antibodies, and immediately analyzed on a flow cytometer. Dextran uptake was calculated as follows (32): ΔgMFI = (gMFI dextran binding at 37°C - gMFI dextran binding at 4°C).

TCGA analysis

The OncoLnc package (37) was used to analyze RNASeqV2 and overall survival data generated by The Cancer Genome Atlas Research Network database (55). OncoLnc was used to conduct survival analyses using multivariate Cox regression modeling, assign logrank p values and Cox coefficients to assess significance, and generate Kaplan-Meier survival curves.

Statistics

Unless otherwise noted in figure legend, data represent mean +/− SEM. Survival curves were analyzed via Mantel-Cox log-rank test unless noted otherwise. All other experiments were compared using parametric 2-tailed student's t-test, chi-square test, or 1-way or 2-way ANOVA, with appropriate corrections for repeated measures of tumor growth curves. All statistical analyses were performed using GraphPad Prism software unless noted otherwise.

Supplementary Material

Refer to Web version on PubMed Central for supplementary material.

Acknowledgments:

We thank P. Ralli-Jain for technical assistance. We thank D. Stetson (U. Washington) for *Tmem173*$^{-/-}$, *Mb21d*$^{-/-}$, and *Mavs*$^{-/-}$ mice, M. Gale Jr. (U. Washington) for *Irf3*$^{-/-}$, *Myd88*$^{-/-}$, *Ticam1*$^{-/-}$, and P14 TCR transgenic mice, and M. Gerner (U. Washington) for OT-I TCR transgenic mice. We thank N. Subramanian (Institute for Systems Biology) for the pSLIK plasmid, and M. Krummel (UCSF) for both the pSIREN-zsGreen plasmid and technical input. We also thank D. Rawlings (Seattle Children's Research Institute) for AAV-related constructs. Reagents described in this manuscript are available from AO for research use under an MTA from the University of Washington.

Funding: This work was supported by NIH grant R01CA228098 and by a Wade F.B. Thompson CLIP award from the Cancer Research Institute, both to AO. AGS was supported by PHS NRSA T32GM007270 and NSF GRFP (DGE-1256082); NWH by T32AI106677–05; MNM by T32CA080416; BPD by F32 AI129254.

References:

1. Binder DC, Fu YX, Weichselbaum RR. Radiotherapy and immune checkpoint blockade: potential interactions and future directions. Trends Mol Med. 21, 463–465 (2015). [PubMed: 26091823]
2. Twyman-Saint Victor C, Rech AJ, Maity A, Rengang R, Pauken KE, Stelekati E, Benci JL, Xu B, Dada H, Odorizzi PM, Herati RS, Mansfield KD, Patsch D, Amaravadi RK, Schuchter LM, Ishwaran H, Mick R, Pryma DA, Xu X, Feldman MD, Gangadhar TC, Hahn SM, Wherry EJ, Vonderheide RH, Minn AJ. Radiation and dual checkpoint blockade activate non-redundant immune mechanisms in cancer. Nature. 520, 373–377 (2015). [PubMed: 25754329]
3. Messmer MN, Snyder AG, Oberst A. Comparing the effects of different cell death programs in tumor progression and immunotherapy. Cell Death Differ. doi:10.1038/s41418-018-0214-4 (2018).
4. Yatim N, Cullen S., Albert ML. Dying cells actively regulate adaptive immune responses. Nat Rev Immunol. 17, 262–275 (2017). [PubMed: 28287107]

5. Orzalli MH, Kagan JC. Apoptosis and necroptosis as host defense strategies to prevent viral infection. Trends Cell Biol. 27, 800–809 (2017). [PubMed: 28642032]
6. Weinlich R, Oberst A, Beere HM, Green DR. Necroptosis in development, inflammation, and disease. Nat Rev Mol Cell Biol. 18, 127–136 (2017). [PubMed: 27999438]
7. Bosurgi L, Hughes LD, Rothlin CV, Ghosh S. Death begets a new beginning. Immunol Rev. 280, 8–25 (2017). [PubMed: 29027219]
8. Kazama H, Ricci JE, Herndon JM, Hoppe G, Green DR, Ferguson TA. Induction of immunological tolerance by apoptotic cells requires caspase-dependent oxidation of high-mobility group box-1 protein. Immunity. 29, 21–32 (2008). [PubMed: 18631454]
9. Akalu YT, Rothlin CV, Ghosh S. TAM receptor tyrosine kinases as emerging targets of innate immune checkpoint blockade for cancer therapy. Immunol Rev. 276, 165–177 (2017). [PubMed: 28258690]
10. Casares N, Pequignot MO, Tesniere A, Ghiringhelli F, Roux S, Chaput N, Schmitt E, Hamai A, Hervas-Stubbs S, Obeid M, Coutant F, Metivier D, Pichard E, Aucouturier P, Pierron G, Garrido C, Zitvogel L, Kroemer G. Caspase-dependent immunogenicity of doxorubicin-induced tumor cell death. J Exp Med. 202, 1691–1701 (2005). [PubMed: 16365148]
11. Tesniere A, Schlemmer F, Boige V, Kepp O, Martins I, Ghiringhelli F, Aymeric L, Michaud M, Apetoh L, Barault L, Mendiboure J, Pignon JP, Jooste V, van Endert P, Ducreux M, Zitvogel L, Piard F, Kroemer G. Immunogenic death of colon cancer cells treated with oxaliplatin. Oncogene. 29, 482–491 (2010). [PubMed: 19881547]
12. Souers AJ, Leverson JD, Boghaert ER, Ackler SL, Catron ND, Chen J, Dayton BD, Ding H, Enschede SH, Fairbrother WJ, Huang DC, Hymowitz SG, Jin S, Khaw SL, Kovar PJ, Lam LT, Lee J, Maecker HL, Marsh KC, Mason KD, Mitten MJ, Nimmer PM, Oleksijew A, Park CH, Park CM, Phillips DC, Roberts AW, Sampath D, Seymour JF, Smith ML, Sullivan GM, Tahir SK, Tse C, Wendt MD, Xiao Y, Xue JC, Zhang H, Humerickhouse RA, Rosenberg SH, Elmore SW. ABT-199, a potent and selective BCL-2 inhibitor, achieves antitumor activity while sparing platelets. Nat Med. 19, 202–208 (2013). [PubMed: 23291630]
13. Kotschy A, Szalvik Z, Murray J, Davidson J, Maragno AL, Le Toumelin-Braizat G, Chanrion M, Kelly GL, Gong JN, Moujalled DM, Bruno A, Csekei M, Paczal A, Szabo ZB, Sipos S, Radics G, Proszenyak A, Balint B, Ondi L, Blasko G, Robertson A, Surgenor A, Dokurno P. Chen I, Matassova N, Smith J, Pedder C, Graham C, Sutdeny A, Lysiak-Auvity G, Girard AM, Grave F, Segal D, Riffkin CD, Pomilio G, Galbraith LC, Aubrey BJ, Brennan MS, Herold MJ, Chang C, Guasconi G, Cauquil N, Melchiore F, Guigal-Stephan N, Lockhart B, Colland F, Hickman JA, Roberts AW, Huang DC, Wei AH, Strasser A, Lessene G, Geneste O. The MCL1 inhibitor S63845 is tolerable and effective in diverse cancer models. Nature. 538, 477–482 (2016). [PubMed: 27760111]
14. Derakhshan A, Chen Z, Van Waes C. Therapeutic small molecules target inhibitor of apoptosis proteins in cancers with deregulation of extrinsic and intrinsic cell death pathways. Clin Cancer Res. 23, 1379–1387 (2017). [PubMed: 28039268]
15. Linkermann A, Green DR. Necroptosis. N Engl J Med. 370, 455–465 (2014). [PubMed: 24476434]
16. Grootjans S, Vanden Berghe T, Vandenabeele P. Initiation and execution mechanisms of necroptosis: an overview. Cell Death Differ. 24, 1184–1195 (2017). [PubMed: 28498367]
17. Scaffidi P, Misteli T, Bianchi ME. Release of chromatin protein HMGB1 by necrotic cells triggers inflammation. Nature. 418, 191–195 (2002). [PubMed: 12110890]
18. Lee BH, Hwang DM, Palaniyar N, Grinstein S, Philpott DJ, Hu J. Activation of the P2X(7) receptor by ATP plays an important role in regulating inflammatory responses during acute viral infection. PLoS ONE. 7, e35812 (2012). [PubMed: 22558229]
19. Love Aaes T, Kaczmarek A, Delvaeye T, De Craene B, De Koker S, Heyndrickx L, Delrue I, Taminau J, Wiernick B, De Groote P, Garg AD, Leybaert L, Grooten J, Bertrand MJ, Agostinis P, Berx G, Declercq W, Vandenabeele P, Krysko DV. Vaccination with necroptotic cancer cells induces efficient anti-tumor immunity. Cell Rep. 15, 274–287 (2016). [PubMed: 27050509]
20. Yatim N, Jusfourgues-Saklani H, Orozco S, Schulz O, Barreira da Silva R, Reis e Sousa C, Green DR, Oberst A, Albert ML. RIPK3 and NF-kB signaling in dying cells determines cross-priming of $CD8^+$ T cells. Science. 350, 328–334 (2015). [PubMed: 26405229]

21. Daniels BP, Snyder AG, Olsen TM, Orozco S, Oguin TH 3rd, Tait SWG, Martinez J, Gale M Jr., Loo YM, Oberst A. RIPK3 restricts viral pathogenesis via cell death-independent neuroinflammation. Cell. 169, 301–313 (2017). [PubMed: 28366204]
22. Nailwal H, Chan FK. Necroptosis in anti-viral inflammation. Cell Death Differ. doi:10.1038/s41418-018-0172-x (2018).
23. Fernald K, Kurokawa M. Evading apoptosis in cancer. Trends Cell Biol. 23, 620–633 (2013). [PubMed: 23958396]
24. Koo GB, Morgan MJ, Lee DG, Kim WJ, Yoon JH, Koo JS, Kim SI, Kim SJ, Son MK, Hong SS, Levy JM, Pollyea DA, Jordan CT, Yan P, Frankhouser D, Nicolet D, Maharry K, Marcucci G, Choi KS, Cho H, Thorburn A, Kim YS. Methylation-dependent loss of RIP3 expression in cancer represses programmed necrosis in response to chemotherapeutics. Cell Res. 25, 707–725 (2015). [PubMed: 25952668]
25. Orozco S, Yatim N, Werner MR, Tran H, Gunja SY, Tait SWG, Albert ML, Green DR, Oberst A. RIPK1 both positively and negatively regulates RIPK3 oligomerization and necroptosis. Cell Death Differ. 21, 1511–1521 (2014). [PubMed: 24902904]
26. Moore MW, Carbone FR, Bevan MJ. Introduction of soluble protein into the class I pathway of antigen processing and presentation. Cell. 54, 777–785 (1988). [PubMed: 3261634]
27. Spranger S, Dai D, Horton B, Gajewski TF. Tumor-residing Batf3 dendritic cells are required for effector T cell trafficking and adoptive T cell therapy. Cancer Cell. 31, 711–723 (2017). [PubMed: 28486109]
28. Sancho D, Joffre OP, Keller AM, Rogers NC, Martinez D, Hernanz-Falcon P, Rosewell I, Reis e Sousa C. Identification of a dendritic cell receptor that couples sensing of necrosis to immunity. Nature. 458, 899–903 (2009). [PubMed: 19219027]
29. Gutierrez KD, Davis MA, Daniels BP, Olsen TM, Ralli-Jain P, Tait SW, Gale M Jr., Oberst A. MLKL activation triggers NLRP3-mediated processing and release of IL-1β independently of gasdermin-D. J Immunol. 198, 2156–2164 (2017). [PubMed: 28130493]
30. Remijsen Q, Goossens V, Grootjans S, Van den Haute C, Vanlangenakker N, Dondelinger Y, Roelandt R, Bruggeman I, Goncalves A, Bertrand MJ, Baekelandt V, Takahashi N, Berghe TV, Vandenabeele P. Depletion of RIPK3 or MLKL blocks TNF-driven necroptosis and switches towards a delayed RIPK1 kinase-dependent apoptosis. Cell Death Dis. 15, e1004 (2014).
31. Mandal P, Berger SB, Pillay S, Moriwaki K, Huang C, Guo H, Lich JD, Finger J, Kasparcova V, Votta B, Ouellette M, King BW, Wisnoski D, Lakdawala AS, DeMartino MP, Casillas LN, Haile PA, Sehon CA, Marquis RW, Upton J, Daley-Bauer LP, Roback L, Ramia N, Dovey CM, Carette JE, Chan FK, Bertin J, Gough PJ, Mocarski ES, Kaiser WJ. RIP3 induces apoptosis independent of pronecrotic kinase activity. Mol Cell. 56, 481–495 (2014). [PubMed: 25459880]
32. Broz ML, Binnewies M, Boldajipour B, Nelson AE, Pollack JL, Erle DJ, Barczak A, Rosenblum MD, Daud A, Barber DL, Amigorena S, Van't Veer LJ, Sperling AI, Wolf DM, Krummel MF. Dissecting the tumor myeloid compartment reveals rare activating antigen-presenting cells critical for T cell immunity. Cancer Cell. 26, 638–652 (2014). [PubMed: 25446897]
33. Salmon H, Idoyaga J, Rahman A, Leboeuf M, Remark R, Jordan S, Casanova-Acebes M, Khudoynazarova M, Agudo J, Tung N, Chakarov S, Rivera C, Hogstad B, Bosenberg M, Hashimoto D, Gnjatic S, Bhardwaj N, Palucka AK, Brown BD, Brody J, Ginhoux F, Merad M. Expansion and activation of CD103+ dendritic cell progenitors at the tumor site enhances tumor responses to therapeutic PD-L1 and BRAF inhibition. Immunity. 44, 924–938 (2016). [PubMed: 27096321]
34. Bottcher JP, Bonavita E, Chakravarty P, Blees H, Cabeza-Cabrerizo M, Sammicheli S, Rogers NC, Sahai E, Zelenay S, Reis e Sousa C. NK cells stimulate recruitment of cDC1 into the tumor microenvironment promoting cancer immune control. Cell. 172, 1022–1037 (2018). [PubMed: 29429633]
35. Boyken SE, Chen Z, Groves B, Langan RA, Oberdorfer G, Ford A, Gilmore JM, Xu C, DiMaio F, Pereira JH, Sankaran B, Seelig G, Zwart PH, Baker D. De novo design of protein homo-oligomers with modular hydrogen-bond network-mediated specificity. Science. 6, 680–687 (2016).
36. Bowles DE., McPhee SW, Li C., Gray SJ, Samulski JJ, Camp AS, Li J, Wang B, Monahan PE, Rabinowitz JE, Grieger JC, Govindasamy L, Agbandje-McKenna M, Xiao X, Samulski RJ. Phase

1 gene therapy for Duchenne muscular dystrophy using a translational optimized AAV vector. Mol Ther. 20, 443–455 (2012). [PubMed: 22068425]

37. Anaya J. OncoLnc: linking TCGA survival data to mRNAs, miRNAs, and lncRNAs. PeerJ Comp Sci. 2, e67 (2016).
38. Daniels BP, Kofman SB, Smith JR, Norris GT, Snyder AG, Kolb JP, Gao X, Locasale JW, Martinez J, Gale M Jr., Loo YM, Oberst A. The nucleotide sensor ZBP1 and kinase RIPK3 induce the enzyme IRG1 to promote an antiviral metabolic state in neurons. Immunity. 50, 64–76 (2019). [PubMed: 30635240]
39. Najjar M, Saleh D, Zelic M, Nogusa S, Shah S, Tai A, Finger JN, Polykratis A, Gough PJ, Bertin J, Whalen M, Pasparakis M, Balachandran S, Kelliher M, Poltorak A, Degeterev A. RIPK1 and RIPK3 kinases promote cell-death-independent inflammation by Toll-like receptor 4. Immunity. 45, 46–59 (2016). [PubMed: 27396959]
40. Saleh D, Najjar M, Zelic M, Shah S, Nogusa S, Polykratis A, Paczosa MK, Gough PJ, Bertin J, Whalen M, Fitzgerald KA, Slavov N, Pasparakis M, Balachandran S, Kelliher M, Mecsas J, Degterev A. Kinase activities of RIPK1 and RIPK3 can direct IFN-β synthesis induced by lipopolysaccharide. J Immunol. 198, 4435–4447 (2017). [PubMed: 28461567]
41. Newton K, Dugger DL, Maltzman A, Greve JM, Hedehus M, Martin-McNulty B, Carano RA, Cao TC, van Bruggen N, Bernstein L, Lee WP, Wu X, DeVoss J, Zhang J, Jeet S, Peng I, McKenzie BS, Roose-Girma M, Caplazi P, Diehl L, Webster JD, Vucic D. RIPK3 deficiency or catalytically inactive RIPK1 provides greater benefit than MLKL deficiency in mouse models of inflammation and tissue injury. Cell Death Differ. 23, 1565–1576 (2016). [PubMed: 27177019]
42. Lee H, Shin EA, Lee JH, Ahn D, Kim CG, Kim JH, Kim SH. Caspase inhibitors: a review of recently patented compounds (2013–2015). Expert Opin Ther Pat. 28, 47–59 (2018). [PubMed: 28885866]
43. Van Hoecke L, Van Lint S, Roose K, Van Parys A, Vandenabeele P, Grooten J, Tavernier J, De Koker S, Saelens X. Treatment with mRNA coding for the necroptosis mediator MLKL induces antitumor immunity directed against neo-epitopes. Nat Commun. 9, 3417 (2018). [PubMed: 30143632]
44. Krysko DV, Denecker G, Festjens N, Gabriels S, Parthoens E, D'herde K, Vandenabeele P. Macrophages use different internalization mechanisms to clear apoptotic and necrotic cells. Cell Death Differ. 13, 2011–2022 (2006). [PubMed: 16628234]
45. Corrales L, Glickman LH, McWhirter SM, Kanne DB, Sivick KE, Katibah GE, Woo SR, Lemmens E, Banda T, Leong JJ, Metchette K, Dubensky TW Jr., Gajewski TF. Direct activation of STING in the tumor microenvironment leads to potent and systemic tumor regression and immunity. Cell Reports. 11, 1018–1030 (2015). [PubMed: 25959818]
46. Park CG, Hartl CA, Schmid D, Carmona EM, Kim HJ, Goldberg MS. Extended release of perioperative immunotherapy prevents tumor recurrence and eliminates metastases. Science Transl Med. 10, doi:10.1126/scitranslmed.aar1916 (2018).
47. Bath-Hextall F, Ozolins M, Armstrong SJ, Colver GB, Perkins W, Miller PS, Williams HC. Surgical excision versus imiquimod 5% cream for nodular and superficial basal-cell carcinoma (SINS): a multicenter, non-inferiority, randomized controlled trial. The Lancet Oncology. 15, 96–105 (2014). [PubMed: 24332516]
48. Kearse M, Moir R, Wilson A, Stones-Havas S, Cheung M, Sturrock S, Buxton S, Cooper A, Markowitz S, Duran C, Thierer T, Ashton B, Meintjes P, Drummond A. Geneious Basic: an integrated and extendable desktop software platform for the organization and analysis of sequence data. Bioinformatics. 28, 1647–1649 (2012). [PubMed: 22543367]
49. Hubbard N, Haing D, Sommer K, Song Y, Khan I, Clough C, Ochs HD, Rawlings DJ, Scharenberg AM, Torgerson TR. Targeted gene editing restores regulated CD40L function in X-linked hyper-IgM syndrome. Blood. 127, 2513–2522 (2016). [PubMed: 26903548]
50. Khan IF, Hirata RK, Russel DW. AAV-mediated gene targeting methods for human cells. Nat Protocol. 6, 482–501 (2011).
51. Sather BD, Romano Ibarra GS, Sommer K, Curinga G, Hale M, Khan IF, Singh S, Song Y, Gwiazda K, Sahni J, Jarjour J, Astrakhan A, Wagner TA, Scharenberg AM, Rawlings DJ. Efficient modification of CCR5 in primary human hematopoietic cells using a megaTAL nuclease and AAV donor template. Sci Transl Med. 7, 307ra156 (2015).

52. Brault M, Olsen TM, Martinez J, Stetson DB, Oberst A. Intracellular nucleic acid sensing triggers necroptosis through synergistic type I IFN and TNF signaling. J Immunol. 200, 2748–2756 (2018). [PubMed: 29540580]

53. Gray EE, Winship D, Snyder JM, Child SJ, Geballe AP, Stetson DB. The AIM2-like receptors are dispensable for the interferon response to intracellular DNA. Immunity. 45, 255–266 (2016). [PubMed: 27496731]

54. Sanjana NE, Shalem O, Zhang F. Improved vectors and genome-wide libraries for CRISPR screening. Nat Methods. 11, 783–784 (2014). [PubMed: 25075903]

55. Weinstein JN, Collisson EA, Mills GB, Shaw KM, Ozenberger BA, Ellrott K, Shmulevich I, Sander C, Stuart JM. The Cancer Genome Atlas pan-cancer analysis project. Nat Genet. 45, 1113–1120 (2013). [PubMed: 24071849]

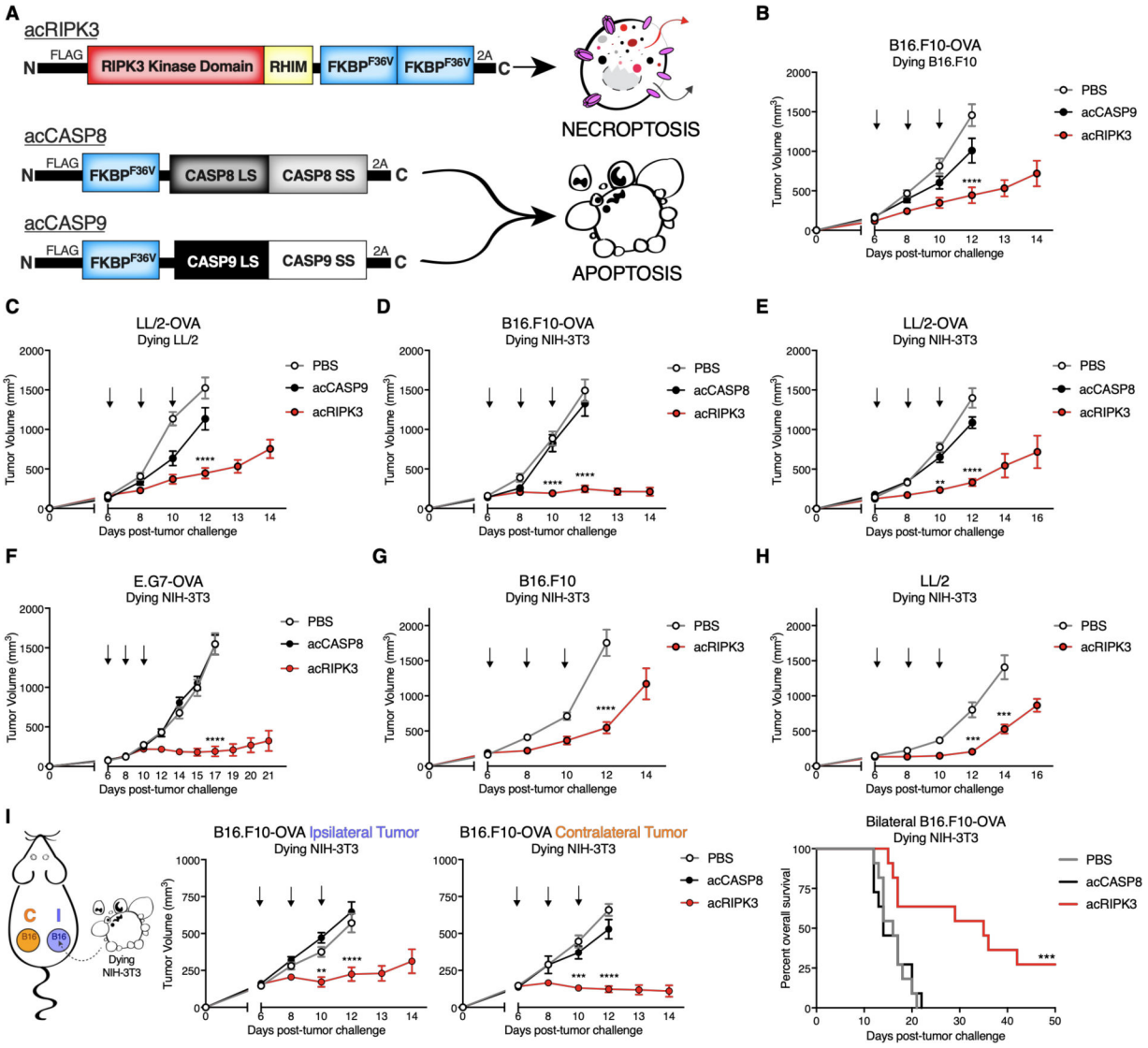

Figure 1: Necroptotic cells confer tumor control across multiple syngeneic flank tumor models.

(**A**) Schematic of pro-death enzyme constructs and respective types of PCD induced downstream following enzyme activation with B/B homodimerizer.

(**B-F**) Tumor growth of B6/J mice bearing (**B,D**) B16.F10-OVA, (**C,E**) LL/2-OVA, or (**F**) E.G7-OVA flank tumors following administration of apoptotic or necroptotic (**B,C**) autologous or (**D-F**) unmatched NIH-3T3 fibroblast cells. N=10–16 mice per group.

(**G,H**) Tumor growth of B6/J mice bearing (**G**) B16.F10 or (**H**) LL/2 flank tumors following administration of necroptotic NIH-3T3 cells. N=9–14 mice per group.

(**I**) Tumor growth of ipsilateral (“I”, treated) and contralateral (“C”, untreated) B16.F10-OVA tumors following administration of either apoptotic or necroptotic NIH-3T3 cells (left, center panels), and survival curve of mice from the same experiment (right panel). N=9–11 mice per group.

**p<0.01, ***p<0.001, ****p<0.0001. Black arrows indicate intratumoral dying cell injections. Error bars represent SEM. Data are pooled from 3–5 independent experiments.

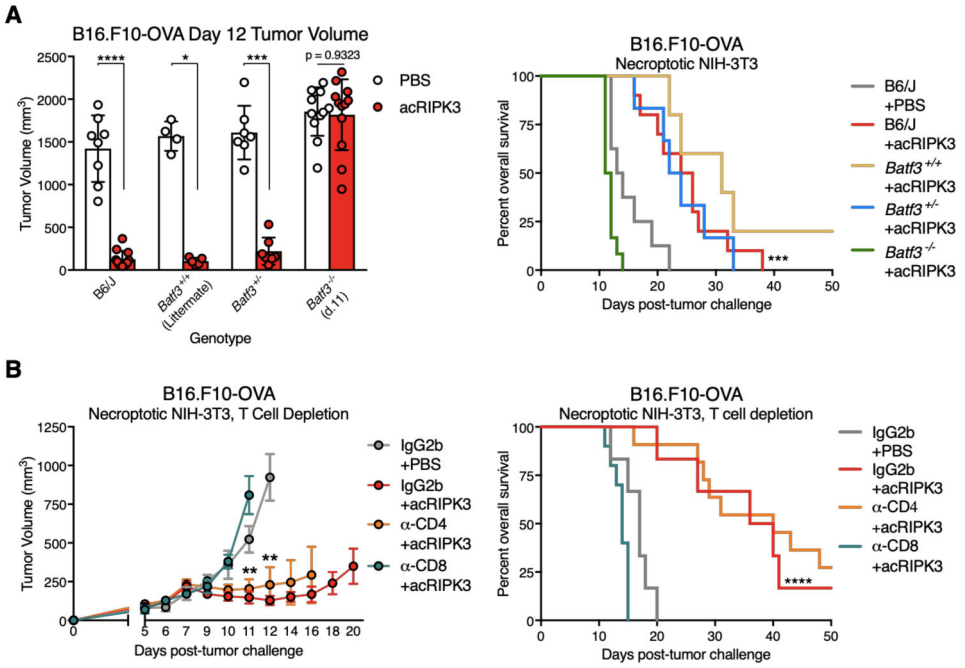

Figure 2: Tumor control by necroptotic cells requires BATF3$^+$ cDC1 and CD8$^+$ leukocytes.

(**A**) Day 12 B16.F10-OVA tumor volumes (left panel) and animal survival (right panel) of mice with varying *Batf3* genotypes following necroptotic fibroblast injections. N=4–12 mice per group.

(**B**) B16.F10-OVA tumor growth (left panel) and animal survival (right panel) upon co-administration of necroptotic fibroblasts with depleting antibodies against either CD4$^+$ or CD8$^+$ leukocytes. N=6–11 mice per group.

*p<0.05, **p<0.01, ***p<0.001, ****p<0.0001. Black arrows indicate intratumoral dying cell injections. Error bars represent SEM. Data are pooled from 2–4 independent experiments.

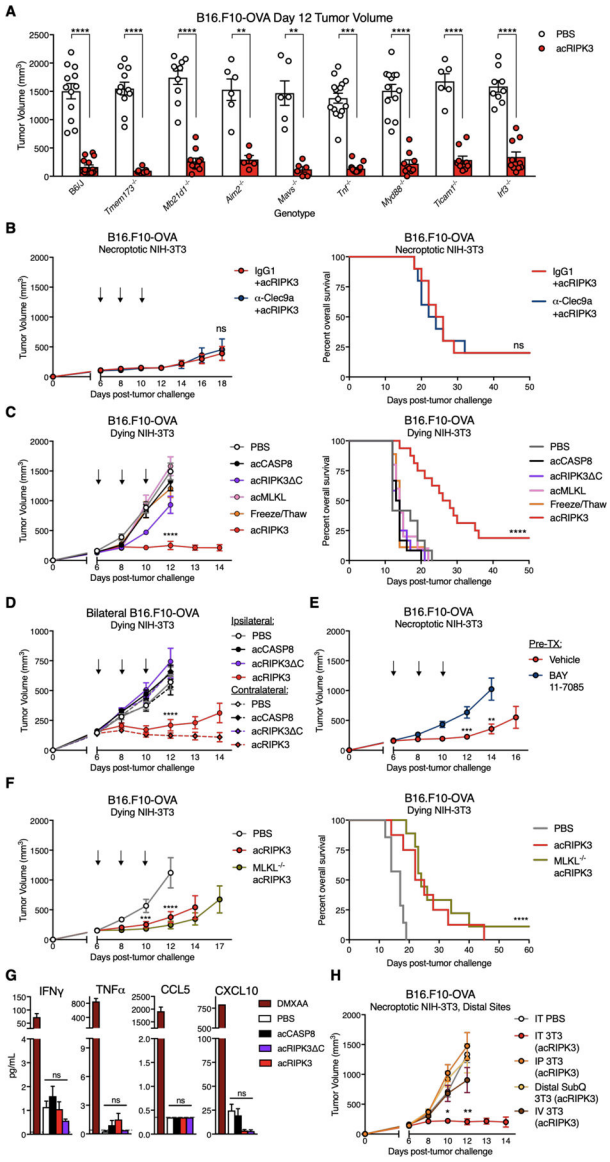

Figure 3: Immune-mediated tumor control by necroptotic cells requires NF-κB activation within dying cells, but not MLKL-mediated cell lysis and DAMP release.

(**A**) Day 12 volumes of B16.F10-OVA tumors in various innate immune knockout mice following necroptotic fibroblast injections on days 6, 8, and 10. N=5–15 mice per group.

(**B**) B16.F10-OVA tumor growth (left panel) and animal survival (right panel) upon co-administration of necroptotic fibroblasts with blocking α-CLEC9A antibody. N=10 mice per group.

(**C**-**D**) Tumor growth and overall survival following administration of lytic necrotic fibroblasts in (**C**) single, or (**D**) contralateral B16.F10-OVA flank tumors. Tumor growth and survival curves for PBS, acCASP8, and acRIPK3 as presented in Figure 1 are also graphed for comparison.

(**E**) B16.F10-OVA tumor growth curves following injection of necroptotic NIH-3T3 fibroblasts pre-incubated with the IκBα phosphorylation inhibitor BAY-117085, which prevents NF-κB activation in treated cells. N=10 mice per group.

B16.F10-OVA tumor growth curves following intratumoral (IT), intraperitoneal (IP), distal subcutaneous (distal subQ), or intravenous (IV) injection of necroptotic fibroblasts. N=7–9 mice per group.

(**F**) B16.F10-OVA tumor growth (left panel) and animal survival (right panel) following IT injection of PBS, necroptotic fibroblasts, or $MLKL^{-/-}$ necroptotic fibroblasts. N=7–9 mice per group.

(**G**) Assessment of systemic inflammation via Luminex assay for inflammatory serum cytokines and chemokines 48h post-intratumoral dying NIH-3T3 injection. DMXAA-injected mice were included as a positive control for systemic inflammatory cytokine production. Gray dotted line represents limit of detection. N=3–5 mice per group.

(**H**) B16.F10-OVA tumor growth curves following intratumoral (IT), intraperitoneal (IP), distal subcutaneous (distal subQ), or intravenous (IV) injection of necroptotic fibroblasts. N=7–9 mice per group.

*p<0.05, **p<0.01, ***p<0.001, ****p<0.0001. Black arrows indicate intratumoral dying cell injections. Error bars represent SEM. Data are pooled from 2–5 independent experiments.

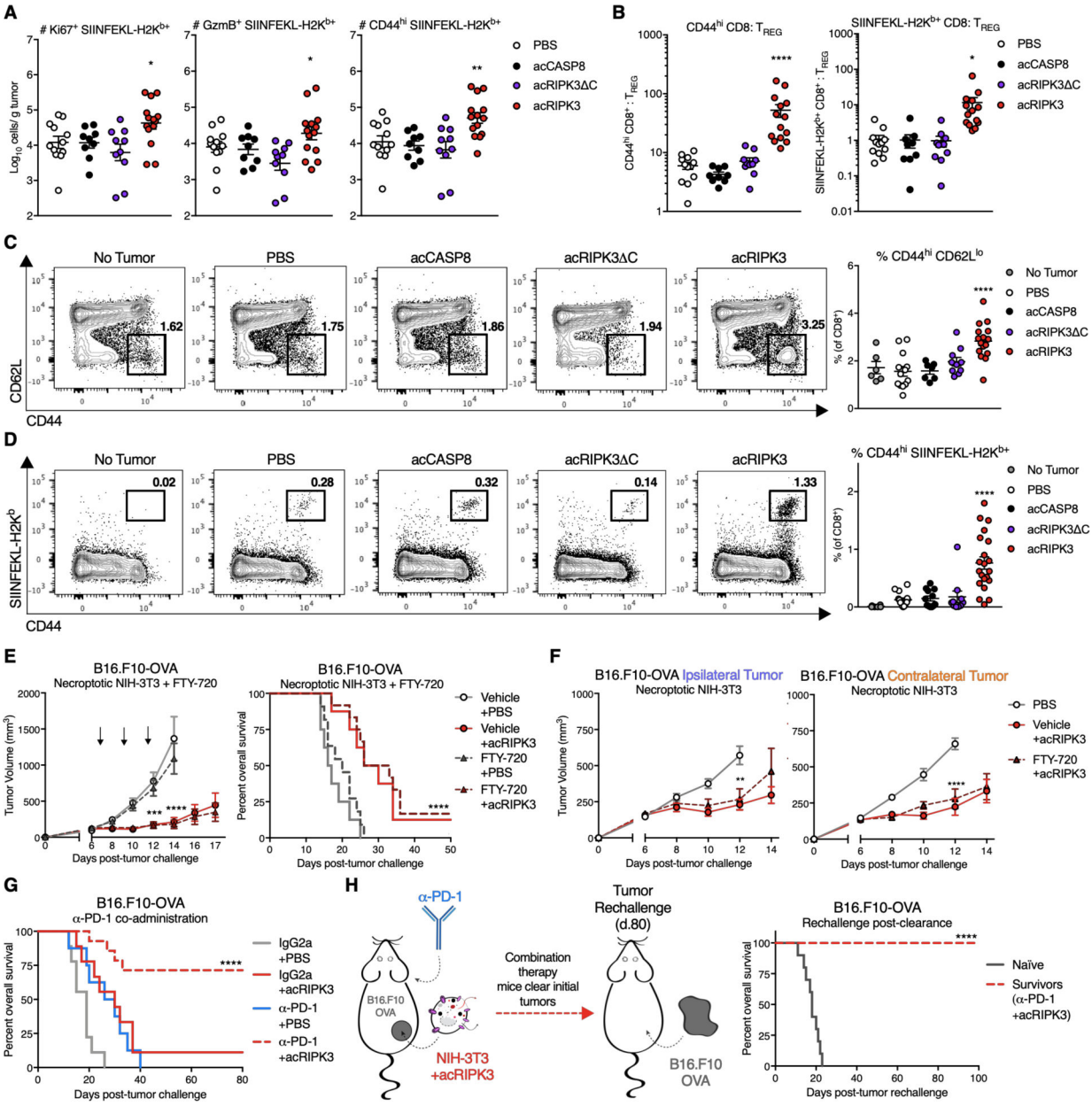

Figure 4: Necroptosis promotes anti-tumor CD8$^+$ T responses and synergizes with immune checkpoint blockade.

(**A**) Absolute numbers of intratumoral CD8$^+$ T cells with various phenotyping markers for proliferation (Ki67), effector function (GranzymeB, GzmB), and activation (CD44), normalized per gram of tumor tissue.

(**B**) Quantification of the ratio of intratumoral activated (CD44^{hi}, left panel) or tumor antigen-specific (SIINFEKL-H2K^{b+}, right panel) CD8$^+$ T cells to immunosuppressive Foxp3$^+$ CD25$^+$ T_{REG}, normalized per gram of tumor tissue.

(**C**) Sample flow plots (left panel) and percentages (right panel) of overall activated CD8$^+$ T cells in the tumor-draining (inguinal) lymph node.

(**D**) Sample flow plots (left panel) and percentages (right panel) of OVA-specific and activated $CD8^+$ T cells in the tumor-draining (inguinal) lymph node.
(**E**) B16.F10-OVA tumor growth (left panel) and animal survival (right panel) following co-administration of necroptotic fibroblasts with the lymphocyte trafficking inhibitor FTY-720. N=8–12 mice per group.
(**F**) Tumor growth of ipsilateral (treated, left panel) and contralateral (untreated, right panel) B16.F10-OVA tumors following administration of necroptotic NIH-3T3 cells with FTY-720. N=9–10 mice per group.
(**G**) Survival curves of B16.F10-OVA tumor-bearing mice following co-administration of necroptotic fibroblasts with the immune checkpoint blockade reagent α-PD-1 or IgG2a isotype. N=8–14 mice per group.
(**H**, left panel) Schematic of tumor re-challenge experiments in mice from (**G**) that successfully clear B16.F10-OVA tumors. (**H**, right panel) Survival of mice re-challenged with B16.F10-OVA cells on the same flank as initial tumor location. N=10 mice per group. *p<0.05, **p<0.01, ***p<0.001, ****p<0.0001. All flow harvests performed 48h post-dying cell injection. Error bars represent SEM. Data are pooled from 2–4 independent experiments.

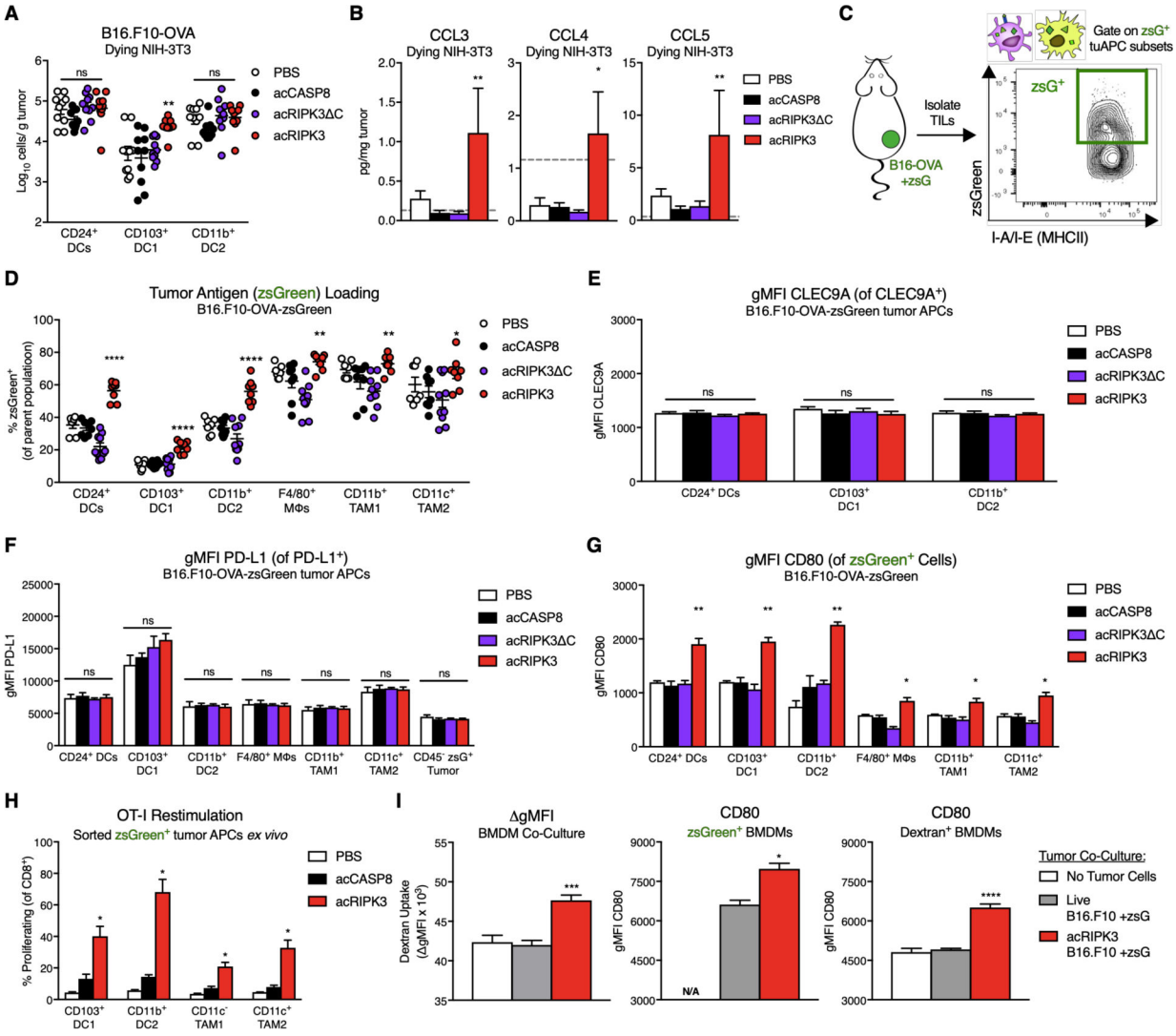

Figure 5: Exposure to necroptosis in the TME promotes antigen uptake and activation of tumor-associated APCs.

(**A**) Absolute numbers of tumor-associated dendritic cell (DC) subsets 48h following intratumoral dying cell administration, normalized per gram of tumor tissue.

(**B**) Intratumoral concentrations of DC-recruiting chemokines 24h post-dying NIH-3T3 injection. Gray dotted line represents limit of detection. N=3–5 mice per group.

(**C**) Experimental schematic of B16.F10-OVA tumor cells expressing zsGreen as a surrogate tumor antigen, allowing for gating on tumor APCs that have phagocytosed tumor antigen.

(**D**) Percent of zsGreen^{+} tumor APCs following dying cell administration.

(**E**) Geometric mean fluorescence intensity (gMFI) of CLEC9A receptor on subsets of tumor DC populations. N=4–6 mice per group.

(**F**) gMFI of PD-L1 on subsets of tumor APC populations and CD45^{-} zsGreen^{+} tumor cells. N=4–6 mice per group.

(**G**) gMFI of the costimulatory marker CD80 on zsGreen^{+} subsets of tumor APC populations. N=3–4 mice per group.

(**H**) Quantification of previously activated OT-I T cell proliferation upon co-culture with zsGreen$^+$ tumor APC subsets sorted *ex vivo* from B16.F10-OVA-zsGreen tumors following dying cell injection. N=3 technical replicates per group, using pooled cells from 5 mice per treatment group.

(**I**) *In vitro* characterization of bone-marrow derived macrophages (BMDMs) co-cultured with live or necroptotic B16.F10-zsGreen tumor cells and dextran-fluorophore beads, assessed for phagocytosis via dextran uptake (left panel), and expression of costimulatory marker CD80 gMFI in zsGreen$^+$ BMDMs (middle panel) or dextran$^+$ beads (right panel). N=3 technical replicates per group.

*p<0.05, **p<0.01, ***p<0.001, ****p<0.0001. All flow harvests performed 48h post-dying cell injection. Error bars represent SEM. Data are representative plots from 1–3 independent experiments (**E-I**), or pooled from 2–3 independent experiments (**A,B,D**).

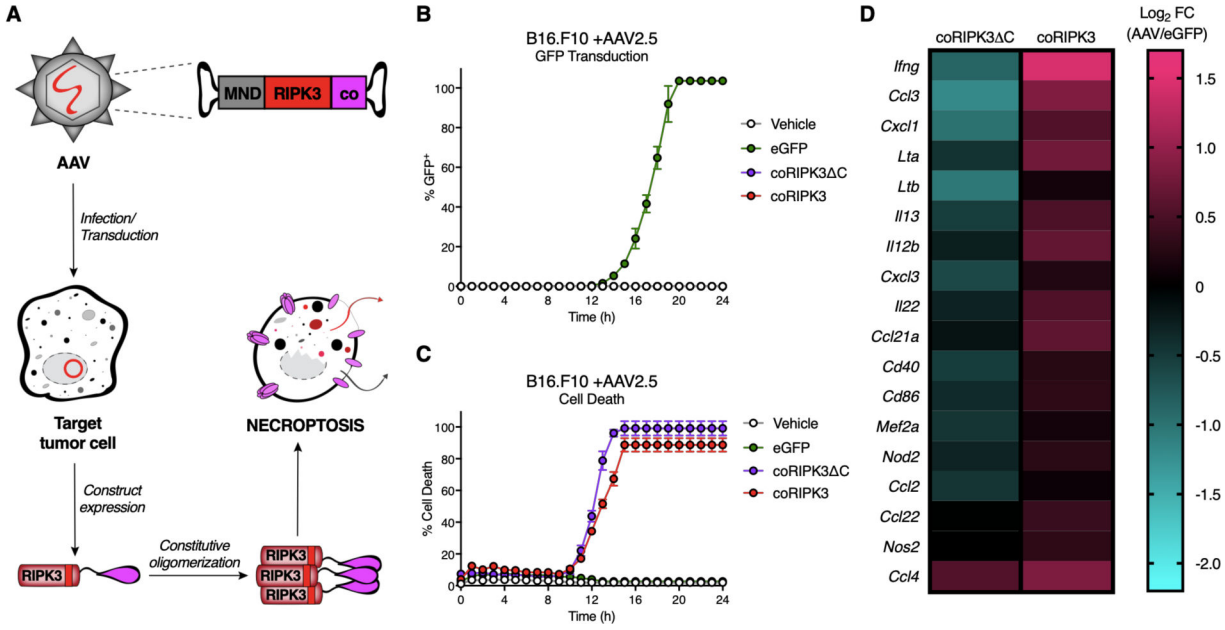

Figure 6: Engineered adeno-associated viruses (AAVs) can be used to specifically induce necroptosis of tumor cells *in vitro*.

(**A**) Schematic of AAVs used to transduce tumor cells to express engineered pro-death enzymes fused to a constitutively-oligomerizing ("co") recruitment domain under the control of a synthetic MND promoter, leading to subsequent induction of a corresponding PCD modality.

(**B,C**) Validation and kinetics of AAV2.5 serotype transduction efficiency in B16.F10 cells *in vitro*. (**B**) Percent of GFP^+ cells transduced with AAV2.5-eGFP control, (**C**) Percent cell death in cells transduced with various death-inducing constructs. N=3 technical replicates per group.

(**D**) Heat map depicting relative expression values of NF-κB-dependent gene targets, chemokines, and cytokines via Nanostring analysis of B16.F10 tumor cells compared to eGFP-transduced controls 10h following AAV2.5 transduction (1×10^{11} IFU).

Data are representative plots from 2 independent experiments (**B,C**), or mean of 3 technical replicates from 1 experiment (**D**).

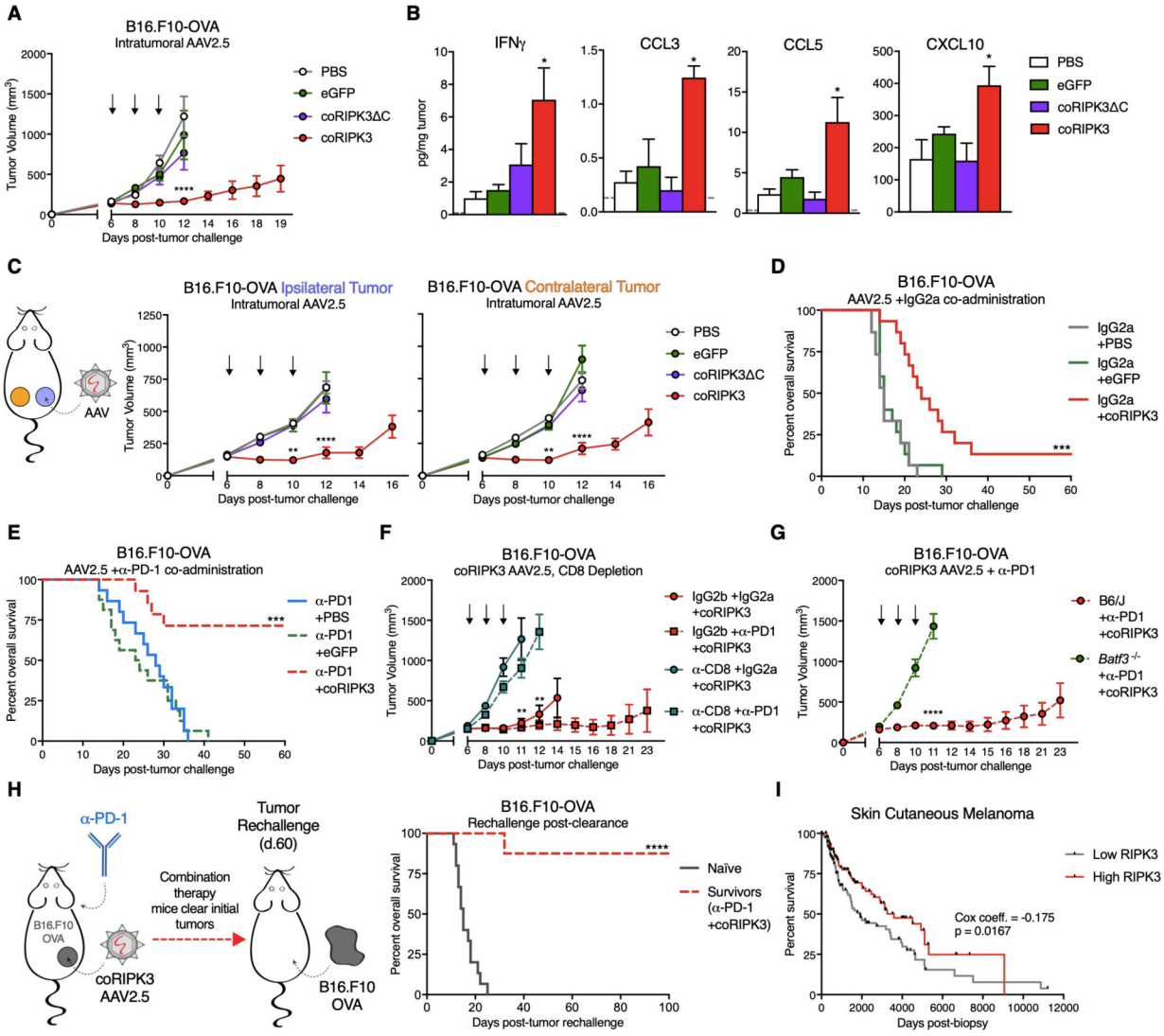

Figure 7: Administration of necroptosis-targeting AAVs in conjunction with α-PD-1 *in vivo* promotes durable tumor clearance.

(**A**) B16.F10-OVA tumor growth curves following intratumoral administration of 1×10^{11} IFU death-inducing AAVs or eGFP control AAV. N=8–14 mice per group.

(**B**) Intratumoral concentrations of inflammatory cytokines and chemokines 48h post-intratumoral AAV injection. Gray dotted line represents limit of detection. N=3–4 mice per group.

(**C**) Tumor growth of ipsilateral ("I", treated) and contralateral ("C", untreated) B16.F10-OVA tumors following AAV administration. N=10–12 mice per group.

(**D**) Survival curves of B16.F10-OVA tumor-bearing mice following co-administration of AAVs with isotype control antibody. N=14–15 mice per group.

(**E**) Survival curves of B16.F10-OVA tumor-bearing mice following co-administration of AAVs with α-PD-1. N=13–16 mice per group.

(**F**) B16.F10-OVA tumor growth upon co-administration of necroptosis-inducing coRIPK3 AAV with α-$CD8^+$ depletion antibody. N=8–10 mice per group.

(**G**) B16.F10-OVA tumor growth in *Batf3* $^{-/-}$ or wild-type control mice following necroptosis-inducing AAV administration. N=10–13 mice per group.
(**H**, left panel) Schematic of tumor re-challenge experiments in mice from (**E**) that successfully clear B16.F10-OVA tumors. (**H**, right panel) Survival of mice re-challenged with B16.F10-OVA cells on the same flank as initial tumor location. N=8–10 mice per group.
(**I**) Kaplan-Meier plot for overall survival of skin cutaneous melanoma patients in TCGA data set. Data are parsed on upper and lower quartiles (25%ile) of RIPK3 mRNA expression. N=114 patients per group.
*p<0.05, **p<0.01, ***p<0.001, ****p<0.0001. Black arrows indicate intratumoral AAV injections. Error bars represent SEM. Data are pooled from 2–4 independent experiments (**A**-**H**).

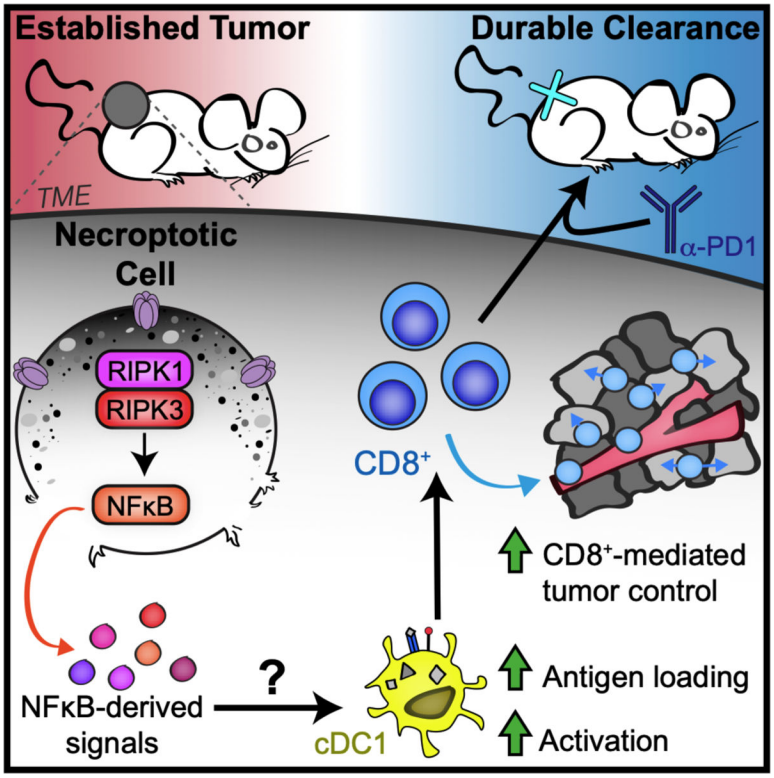

Figure 8: Proposed model by which necroptotic cell death within the tumor microenvironment promotes anti-tumor immunity.

RIPK1/RIPK3 activation in necroptotic cells produces NF-κB-dependent signals that promote $CD103^+$ cDC1 and $CD8^+$ leukocyte-mediated anti-tumor immunity, which synergizes with α-PD1 to promote durable tumor clearance.